Spring 5-2021

Examining Summertime Melt and Temperatures in the North Pacific Cordillera

Ingalise Kindstedt
University of Maine, ingalise.kindstedt@maine.edu

EXAMINING SUMMERTIME MELT AND TEMPERATURES IN THE NORTH PACIFIC CORDILLERA

By

Ingalise Kindstedt

B.S. Georgetown University, 2019

A THESIS

Submitted in Partial Fulfillment of the

Requirements for the Degree of

Master of Science

(in Quaternary and Climate Studies)

The Graduate School

The University of Maine

May 2021

Advisory Committee:

Karl Kreutz, Professor of Earth and Climate Sciences, Advisor

Dominic Winski, Research Assistant Professor of Earth and Climate Sciences

Kristin Schild, Research Assistant Professor of Earth and Climate Sciences

EXAMINING SUMMERTIME MELT AND TEMPERATURES IN THE NORTH PACIFIC CORDILLERA

By Ingalise Kindstedt

Thesis Advisor: Dr. Karl Kreutz

An Abstract of the Thesis Presented
in Partial Fulfillment of the Requirements for the
Degree of Master of Science
(in Quaternary and Climate Studies)
May 2021

Temperature changes in glaciated regions are of immediate concern for estimates of future sea level rise. Alaska and the surrounding region contain over 40 mm of potential sea level rise in its many alpine glaciers, which are experiencing some of the highest rates of mass loss globally. However, records of both past and present temperatures in the region's alpine sectors are sparse and limited in temporal and spatial extent. Here I examine the application of MODIS land surface temperatures and layers of refrozen melt in ice cores as temperature indicators in the St. Elias and Alaska Ranges. First, I find that a previously observed cold bias in MODIS LSTs relative to in situ temperatures is likely due to a discrepancy between surface and air temperatures over glaciated surfaces. The bias is not a result of MODIS' large footprint (1 km2), nor is it introduced by poorly constrained snow emissivity values used in the LST calculation, although the role of emissivity in its amplification remains unknown. Although MODIS LSTs may be used to supplement in situ temperatures, factors affecting the relationship between surface and air temperatures must be accounted for. Second, I find that melt layers since 2000 in an ice core from Eclipse Icefield (St. Elias Range) do not correspond to years of high temperatures. However, years of high surface ablation do, suggesting that complex percolation dynamics, rather than the surface environment, control the preservation of an annual melt record in ice cores.

Although modern melt layers do not reflect temperature, Eclipse may transition between percolation regimes with modest temperature changes and melt layers from the pre-industrial Holocene may yet provide a valuable record of past temperatures. Lastly, I find that a novel analytical technique for melt layer identification using bubble number density agrees with established methods, validating their continued use. Although bubble number density cannot be used to unequivocally identify highly thinned melt layers at depth, the method shows promise with improved accuracy in depth measurements and signal-to-noise ratio.

EXAMINING SUMMERTIME MELT AND TEMPERATURES IN THE NORTH PACIFIC CORDILLERA

By Ingalise Kindstedt

Thesis Advisor: Dr. Karl Kreutz

A Lay Abstract of the Thesis Presented
in Partial Fulfillment of the Requirements for the
Degree of Master of Science
(in Quaternary and Climate Studies)
May 2021

Measuring warming of regions with glaciers is a critical component of estimating future sea level rise. Alaska and the surrounding region contain many rapidly shrinking alpine glaciers, which hold over 40 mm of potential sea level rise. However, very few temperature records exist in the region, especially in its remote mountain ranges. Here I examine whether land surface temperatures obtained from MODIS satellite data and layers of refrozen melt in ice cores can be used as temperature indicators in the St. Elias and Alaska Ranges, where weather stations are few or absent. First, I find that MODIS land surface temperatures tend to be colder than weather station measurements, likely because of a difference between surface and air temperatures over snow-covered surfaces. Factors causing a discrepancy between air and surface temperatures must be considered when using MODIS surface temperatures instead of, or in addition to, weather station measurements. Second, I find that layers of refrozen melt formed since 2000 in an ice core at Eclipse Icefield (St. Elias Range) do not line up with years of high temperatures. However, warm years do experience more melt at the surface, so the ice core record seems to be controlled by how far melt can percolate through the snow, rather than how much is formed on the surface. Although modern melt layers do not line up with years of high temperatures, the

percolation environment at Eclipse may have been different during much of the cooler pre-industrial Holocene, and melt layers from these periods may provide valuable temperature information. Lastly, I find that measuring the number of bubbles in ice cores may provide a useful tool for identifying layers of refrozen melt that have been squeezed too thin to pick out visually. However, doing so will require a measurement technique that does not call for the ice being shaved into thin sections, as this process introduces uncertainty in depth measurements and results in a very small amount of bubbles actually being sampled.

ACKNOWLEDGEMENTS

Lastly, thank you to my family and friends scattered across the country for being excited that I'm excited about ice, and to the community of skiers, climbers, science nerds, and all-around great people that have made Orono home.

TABLE OF CONTENTS

LIST OF TABLES

LIST OF FIGURES

LIST OF ABBREVIATIONS

MCA Medieval Climate Anomaly

MODIS MODerate resolution Imaging Spectroradiometer

LST Land Surface Temperature

PDD Positive Degree Day

AWS Automated Weather Station

ASTER Advanced Spaceborne Thermal Emissions Radiometer

TIR Thermal Infrared

LS Landsat

TES Temperature-Emissivity Separation

UCC Unit Conversion Coefficient

DN Digital Number

BT Brightness Temperature

GPR Ground Penetrating Radar

AppEEARS Application for Extracting and Exploring Analysis Ready Samples

HTM Holocene Thermal Maximum

LLS Laser Light Scattering

MADGE Maine Automated Density Gauge Experiment

GRIP GReenland Ice core Project

CHAPTER 1

CLIMATE AND GLACIER MASS BALANCE IN THE NORTH PACIFIC

1.1 Background

The behavior of glaciers and ice caps worldwide in response to rising air temperatures is a crucial control on the timing and magnitude of current and future global sea level rise. From 1961 to 2016, glaciers and ice caps (excluding Greenland and Antarctica) contributed 27 ± 22 mm to global mean sea level (g.m.s.l) rise, or approximately 25-30% of the total observed sea level rise over that time period (Zemp et al. 2019). Alaskan glaciers alone accounted for nearly one third (8 mm) of this increase, and are predicted to contribute another 19 ± 4 mm to global sea level by 2100 (Zemp et al. 2019; Wahr, Burgess, and Swenson 2016). Glaciers in Alaska and the greater North Pacific cordillera are vulnerable to enhanced high elevation temperature increases, most likely due to warming in the free troposphere (Williamson et al. 2020). Here I use the term "North Pacific" to refer to the region of North America along the most northern reaches of the Pacific Ocean, specifically Alaska, as well as parts of neighboring Yukon Territory and British Columbia. I use the term "North Pacific cordillera" to refer to high elevation sectors of this region. The cordillera contains the majority of the world's non-polar ice, representing 43.3 ± 11.2 mm of potential global sea level rise, thus making summer temperatures in the region a matter of great concern for future sea level predictions (Arendt et al. 2002; Farinotti et al. 2019).

In addition to its importance to sea level rise, glacier mass balance in the North Pacific has marked effects on hydrology, ecology, and local human communities. For example, the Kaskawulsh Glacier flows from its head in the St. Elias icefields into two rivers, the Kaskawulsh and the Slims (Clarke and Holdsworth 2002). Depending on local conditions and the position of its terminus, the glacier contributes varying amounts of water to each river, profoundly influencing local and regional hydrology, as the Kaskawulsh River drains to the Pacific Ocean while the Slims River feeds the Kluane Lake ecosystem and eventually
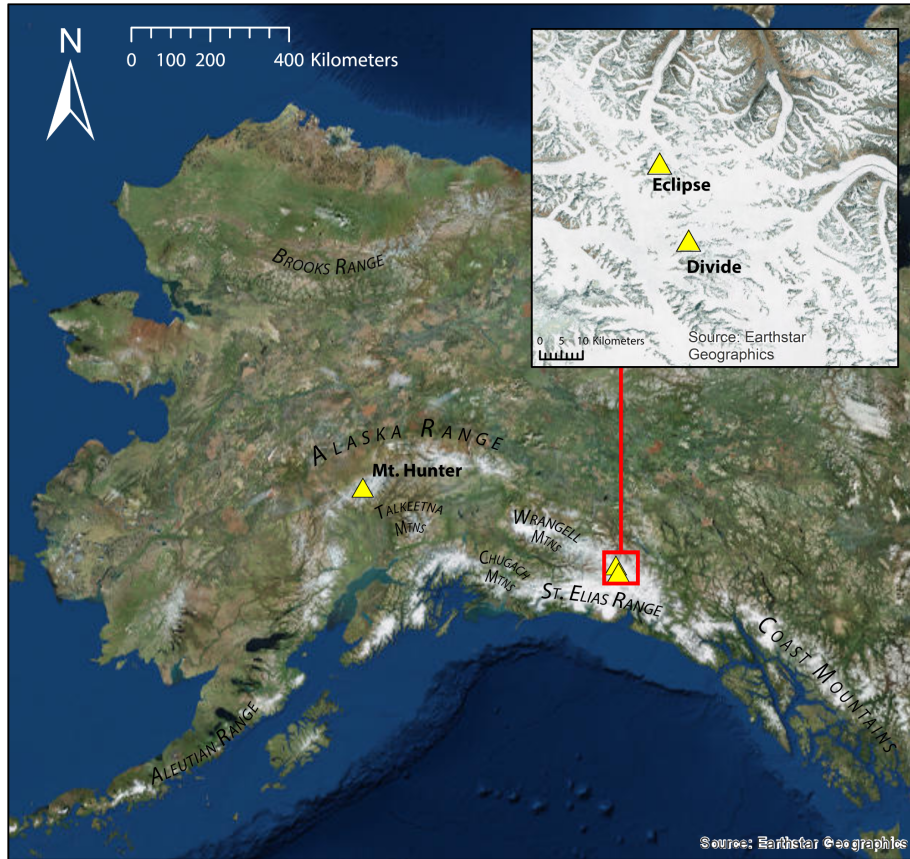
Figure 1.1. Study sites in the North Pacific region. Mountain ranges over 2,500 m a.s.l. are labeled. Study sites (yellow triangles) are located in the region's two highest ranges, the Alaska and the St. Elias. The elevations of the Mt. Hunter summit plateau, Eclipse Icefield and Icefield Divide are 3,900 m a.s.l., 3,017 m a.s.l., and 2,603 m a.s.l. respectively (Winski et al. 2018; McConnell 2019).

drains to the Arctic Ocean (Clarke and Holdsworth 2002). Nearby Donjek Glacier, a surge-type glacier, has historically dammed the Donjek River during surges; outburst floods from the resultant lake put a portion of the Alaska highway at risk (Clarke and Holdsworth 2002). Outburst floods from other glacier-dammed lakes put various human communities at risk throughout the North Pacific region. For example, the town of McCarthy, Alaska lies in part in the floodplains of the Kennicott River and McCarthy Creek, which have experienced repeated episodes of flooding due to outbursts from glacier-dammed lakes (Jones and Glass 1993). Despite its regional and global importance, the North Pacific cordillera remains poorly studied, largely due to its remote, rugged

nature, which makes it extremely difficult to access for in situ temperature measurements. Our understanding of the past and present climatic behavior of North Pacific high elevation sectors therefore relies heavily on proxy records and remote sensing products. Here, I aim to extend the spatial and temporal coverage of modern and paleo temperature records. Study sites Mt. Hunter (62.93°N, 151.08°W, 3,910 m a.s.l.), Eclipse Icefield (60.84°N, 139.84°W, 3,017 m a.s.l; hereafter referred to as "Eclipse"), and Icefield Divide (60.68°N, 139.78°W, 2,603 m a.s.l; hereafter referred to as "Divide") are shown in Figure 1.1. The time periods covered by all datasets used in this study are shown in Fig. 1.2 .
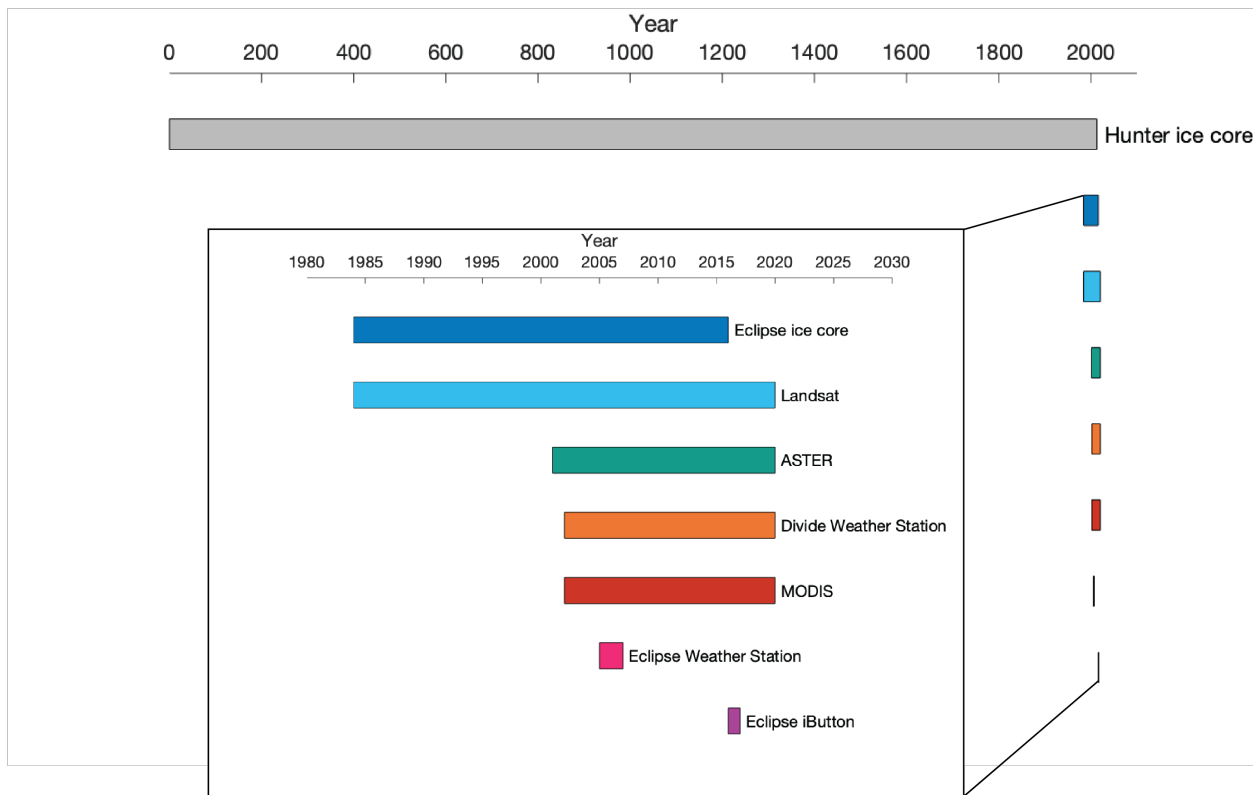
Figure 1.2. Temporal coverage of datasets during the past 2,000 years used in this study. The Hunter ice core covers the entire Common Era (full length of 8,000 years not shown). Inset shows detail of modern records since the twentieth century. The time periods covered by the modern records are 1984-present (Landsat), 1984-2016 (Eclipse ice core), 1999-present (ASTER), 2002-present (Divide weather station), 2002-present (MODIS), 2005-2007 (Eclipse weather station), and 2016-2017 (Eclipse iButton).

3

1.2 Goals

Broadly, I aim to elucidate past and present temperature trends in the St. Elias Range (hereafter referred to as "the St. Elias") and greater North Pacific region, and their relationship to glacier mass balance. The specific goals of this project are as follows: to supplement the limited available in situ temperature records in the St. Elias with reliable remote sensing datasets (Chapter 2), to determine whether melt layers in the St. Elias are associated with periods of surface warmth (Chapter 3), and to produce a robust temperature record extending back through the Medieval Climate Anomaly (MCA) (Chapter 4). The supplementing of in situ temperature records with remote sensing datasets is motivated by the need to monitor current temperature trends and glacier response in the St. Elias. Doing so will additionally aid in the interpretation of an ice core drilled at Eclipse Icefield in 2016 by extending our very limited modern temperature record at the site (2005-2007, 2016-2017). My approach is to identify the cause of an observed bias in NASA's MODerate resolution Imaging Spectroradiometer (MODIS) land surface temperature (LST) product in order to enable the development of an effective correction. The determination of whether melt layers in the St. Elias are associated with periods of surface warmth is motivated by the prospective utility of these layers as indicators of past climate. In order to confidently interpret past melt features at a given site in terms of climate, we need to ensure that we understand which components of the climate system present melt features reflect. My approach is to relate melt layers in a shallow ice core at Eclipse to records of temperatures and positive degree days (PDDs) at the site. The production of a robust temperature record extending through the MCA is motivated by the need to contextualize current warming and the potential of a useful analog through which we can study regional processes. My approach is to develop a method for bubble density analysis of melt features in the lower portion of the Hunter core, expanding beyond established optical analysis techniques used on the upper core.

CHAPTER 2

MODIS LAND SURFACE TEMPERATURES IN THE ST. ELIAS RANGE

2.1 Background and Goal

The North Pacific cordillera contains over 40 mm of global sea level rise in small alpine glaciers vulnerable to atmospheric warming (Farinotti et al. 2019). Widespread monitoring of air temperatures and glacier response is crucial to predicting both local hydrological changes and future sea level rise. The most direct way to do this is by taking in situ measurements, for example, with a weather station. Weather stations are an invaluable tool where they can be deployed because they provide direct measurements of a number of variables (e.g. air temperature, wind speed, solar radiation, humidity, etc.) for a specific point in space at a very high temporal resolution (often hourly). However, while glaciers in the North Pacific tend to be located in the cordillera itself, most weather stations are found in nearby lower elevation areas (e.g. 610 m a.s.l. at Haines Junction, 806 m a.s.l. at Burwash Landing; Fig. 2.1). Lower elevation sites receive moisture from different air masses and are sensitive to different sources of variability than their high elevation counterparts, so data from these stations is not necessarily representative of climatic behavior in the cordillera (McConnell 2019). In particular, low elevation sites are primarily sensitive to local climate, while higher elevation sites are sensitive to atmospheric circulation patterns on a large spatial scale. For example, melt on Mt. Hunter (Alaska Range) has been correlated with high sea surface temperatures as far away as the central tropical Pacific (Winski et al. 2018). Additionally, low-elevation weather stations likely underestimate the warming experienced at nearby higher elevation sites. Modeling studies (Chen, Chao, and Liu 2003; Giorgi et al. 1997) predict that warming rates increase with elevation, a prediction that is borne out by observation in a variety of ranges including the St. Elias and greater North Pacific cordillera (Williamson et al. 2020; Diaz, Bradley, and Ning 2014; Pepin et al. 2015; Rangwala and Miller 2012).
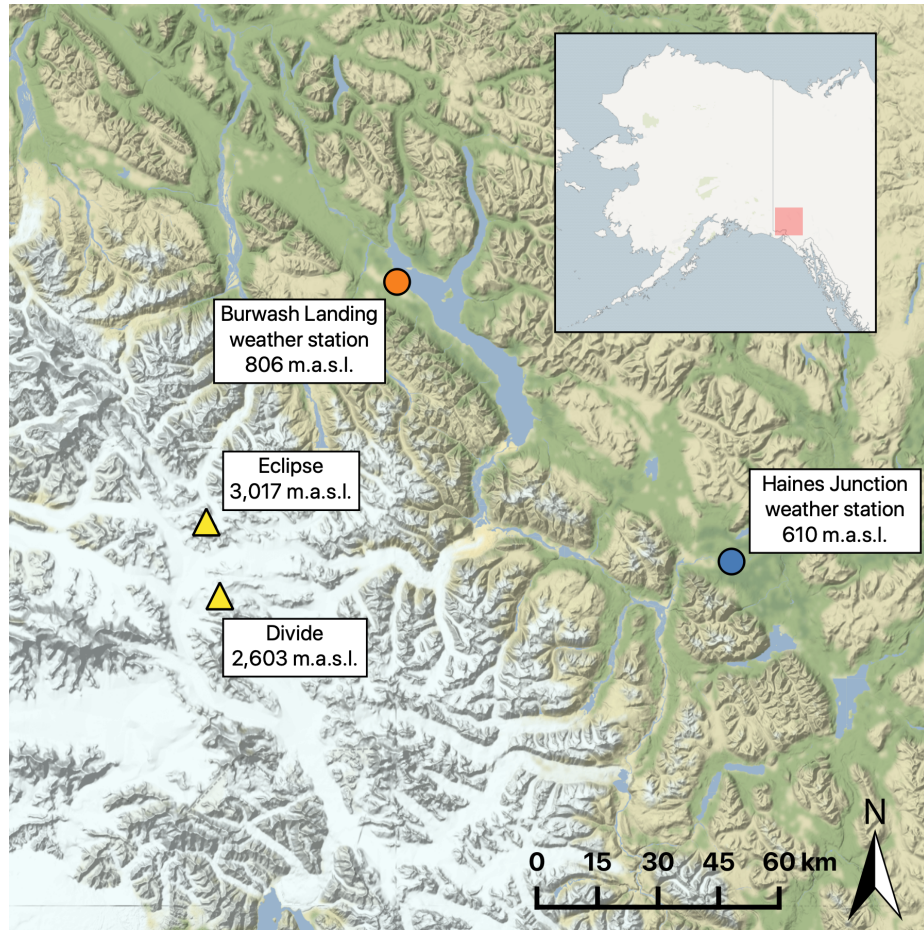
Figure 2.1. Study sites Eclipse and Divide and nearby weather station locations at Burwash Landing and Haines Junction

Due to the inaccessibility of the North Pacific cordillera for in situ measurements, our understanding of the region's climatic behavior relies heavily on remote sensing products, such as MODIS LSTs. Unlike weather stations, which measure air temperature (typically 2 m above the surface), MODIS LSTs record the temperature of the surface itself. Although these two variables are closely related, they are distinct and their values can differ. MODIS LSTs have exhibited a cold bias relative to local (high elevation) weather station temperature measurements in the Upper Kaskawulsh-Donjek region of the St. Elias Range (weather station located at Divide; Williamson et al. 2014). However, it is unclear if this discrepancy is a real temperature difference between the surface and air, or if it results from the instrumentation and algorithm used to produce MODIS LSTs. If MODIS LSTs are to

6

supplement our spatially and temporally limited modern in situ data in the St. Elias, it's crucial that we understand the relationship between "skin" (surface) and air temperature in the region, and that we identify and correct for inaccuracies in the temperature product.

The goal of this chapter is to identify the primary cause of the cold bias in MODIS LSTs in the St. Elias Range. To achieve this goal, I address the following questions:

1. Is the MODIS LST cold bias a real temperature difference between the surface and air due to near-surface temperature inversions?

2. Is the MODIS LST cold bias due to the large spatial footprint of the MODIS sensor in highly heterogeneous alpine terrain?

3. Is the MODIS LST cold bias due to poorly constrained snow emissivity values?

Near-surface temperature inversions, where the surface is colder than the air directly above it, develop over glaciated regions when heat transfer from the surface to the air occurs as a result of an energy imbalance at the surface-air interface (Adolph, Albert, and Hall 2018), and have long been documented over glaciated regions in both hemispheres (Reeh 1991; Kahl 1990; Overland and Guest 1991; Phillpot and Zillman 1970). However, most of these studies use 2 m air temperature as the base, rather than the top, of the inversion, thereby ignoring the skin temperature altogether. For example, inversions based at 2 meters have been observed over both Greenland (Miller et al. 2013) and Antarctica (Hudson and Brandt 2005), especially during winter months. These large-scale inversions (2-22 m high in the atmosphere) have been attributed to the difference between snow surface emissivity and atmospheric emissivity when the amount of absorbed incoming solar radiation is small, such as during the polar winter (Hudson and Brandt 2005). Smaller-scale near-surface inversions have also been observed across a variety of settings. For example, surface temperatures at the South Pole during the winter of 2001 were a median of 1.3°C lower than 2 m air temperatures under clear sky conditions (Hudson and Brandt 2005). Likewise, during June-July 2015, skin temperatures at Summit, Greenland

were often significantly lower (by 0.32-2.4°C) than 2 m air temperatures (both measured in situ), particularly at low wind speeds and low values of incoming solar radiation (Adolph, Albert, and Hall 2018). In addition, surface temperatures measured in situ at Summit during 2008-2009 were on average 1.5 ± 0.2°C lower than coincident 2 m air temperatures (Koenig and Hall 2010). MODIS LSTs over the same period were an average of 5.5°C lower than coincident 2 m air temperatures, amounting to an $\sim$3°C cold bias in the MODIS LSTs once the difference between skin and air temperatures is accounted for (Koenig and Hall 2010). In contrast, generally good agreement between LSTs and 2 m air temperatures (both measured in situ) has been documented over three Alaskan sites: Barrow and Atqasuk in 2010, and Olitok Point in 2014 (Good 2016). Agreement increased with greater snow cover at these sites in the winter (Good 2016). In the summer, clear-sky LSTs were found to be higher than corresponding 2 m air temperatures, likely due to the high sensitivity and rapid response of LST to insolation (Good 2016). In the St. Elias, paired in situ skin and air temperatures are absent; our understanding of the relationship between the two is therefore extremely limited. If inversions account for the majority of the apparent cold bias in MODIS LSTs, future work should focus on understanding near-surface thermal processes rather than refining the MODIS instrumentation.

Alternatively, the cold bias could result from inaccuracies generated during the production of MODIS LSTs. Unlike the interior of large ice sheets, the St. Elias Icefields are characterized by marked heterogeneity in surface type, elevation, aspect, incline, wind scouring, and shading (note the many ridges and nunataks shown in figure 2.2). All of these variables can affect surface temperature and cause it to vary over meters or tens of meters. The spatial resolution of MODIS (1 km) may be too coarse to capture such spatial variation, and the average temperature value over a square kilometer may not accurately represent individual surface temperatures at particular locations within the pixel. Like surface conditions, surface emissivity values are also highly heterogeneous and remain poorly constrained in snow-covered regions regions (Hori et al. 2006; Hulley, Veraverbeke,

and Hook 2014; Shea and Jamieson 2011). Emissivity is a measure of how effectively a surface emits radiation and is used in the MODIS algorithm to calculate surface temperature from radiances. Since snow does not emit radiation uniformly, emissivity is not uniform across snow surface types; rather it decreases with increasing particle size and increasing density (which can occur due to either packing or welding of grains), and it increases with the presence of meltwater (Salisbury, D'Aria, and Wald 1994). In the 10.5-12.5 μm range (MODIS bands 31 and 32), emissivity can vary from 0.949 to 0.997 depending on the surface type (fine dendrite snow, medium granular snow, coarse grain snow, sun crust, and bare ice), with lower emissivity values for coarse grain snow and ice than for fine dendrite snow (Wan and Zhang 1999; Hori et al. 2006). Snow surface type varies spatiotemporally in the St. Elias icefields; compaction processes and surface melt occur heterogeneously over the variable terrain and could lead to disparate changes in surface emissivity over hours to days.

2.2   Methods

2.2.1   Study Sites and Datasets

In situ and MODIS temperature data were collected at study sites Divide and Eclipse (Fig. 1.1). Site specifications can be found in Chapter 1. In situ temperatures at Divide were obtained from an Automated Weather Station (AWS) at the site. The Divide temperature record includes Campbell 107F temperature probe hourly readings ($\pm$ 0.2°C) from 2002-2015 and HOBO S-THB-M008 12-bit sensor hourly readings ($\pm$ 0.21°C) from 2009-present. In situ temperatures at Eclipse were obtained from an AWS from 2005-2007, and a Maxim Integrated iButton Data Logger DS1922L ($\pm$ 0.5°C) from May 21, 2016 to May 17, 2017. The iButton recorded temperatures at 3-hour intervals and was placed inside a plastic container on a bedrock outcrop $\sim$3 km from the site of an ice core drilled at Eclipse in 2016. I combined the Eclipse AWS and iButton datasets, as the MODIS cold biases computed with each were comparable in magnitude.
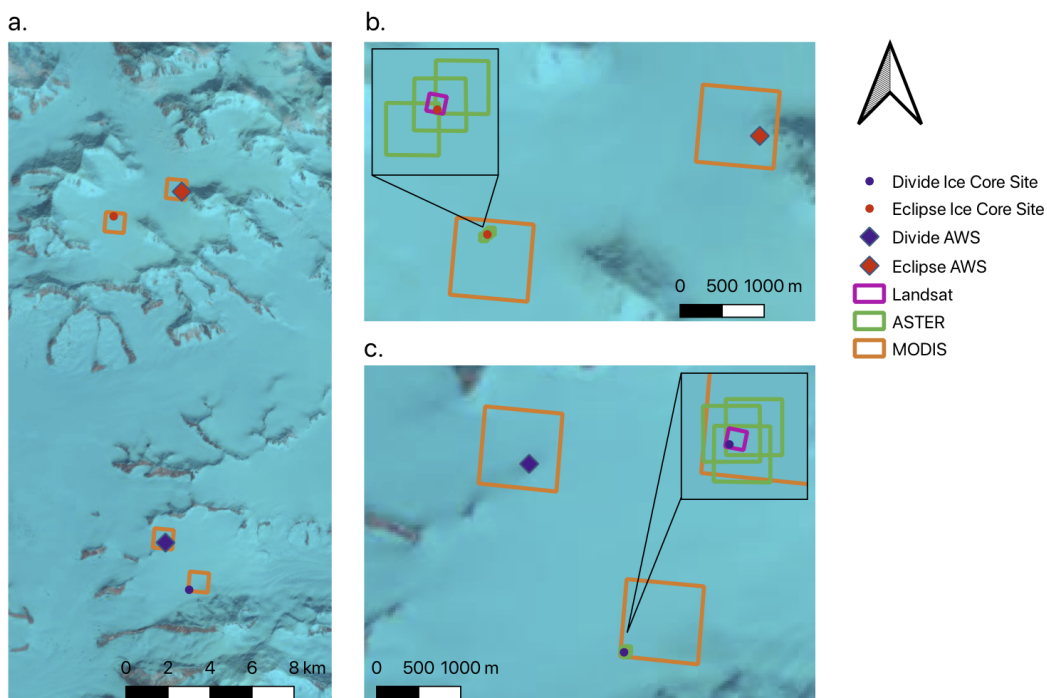
Figure 2.2. MODIS, ASTER, and Landsat footprints at Eclipse and Divide ice core and AWS sites. a) Upper Kaskawulsh-Donjek area containing Eclipse and Divide sites, b) Eclipse ice core and AWS sites, c) Divide ice core and AWS sites. Imagery from Landsat 8.

To compare the AWS data against remote sensing measurements of temperature, I consider thermal infrared (TIR) data from three different NASA sensors: MODIS, Advanced Spaceborne Thermal Emissions Radiometer (ASTER), and Landsat. The time periods covered by all datasets used in this study are shown in Figure 1.2. Wavelength ranges of all thermal infrared (TIR) bands used are shown in Table A.1.

Previous studies of MODIS LSTs (Williamson et al. 2014; McConnell 2019) identified a cold bias in the MOD11 LST product; however, the MODIS MOD21 and MYD21 (together referred to as MxD21) products superseded the MOD11 and MYD11 (together referred to as MxD11) products in 2017, so a new assessment should be conducted. Both sets of

products use emissivity values to calculate LSTs. However, the MxD21 products use the Temperature-Emissivity Separation (TES) algorithm originally developed for ASTER to dynamically retrieve emissivity values for each pixel, rather than assigning fixed emissivity values based on land cover type, as was done in the split-window algorithm used to calculate the MxD11 products (Hulley 2017). The dynamically retrieved MxD21 emissivity values corrected for MxD11 cold biases over barren surfaces (Li et al. 2020; Yao et al. 2020). However, I find the correction does not hold over snow- and ice-covered surfaces; MYD21 LSTs contain the same cold bias as their predecessors (Fig.2.3). The prefix "MOD" denotes data from the MODIS instrument housed on the Terra satellite; the prefix "MYD" denotes data from the MODIS instrument housed on the Aqua satellite. Only MYD21 was used to test the cold bias because MOD21 was discontinued due to an optical crosstalk issue in the infrared bands (Hulley 2017).

I test for the cold bias using MYD21 data from Eclipse and Divide ice core sites, which are approximately 3 km from the nearest in situ measurements (Fig. 2.2). To ensure comparability between in situ (AWS and iButton) and ice core sites, I compared MYD21 temperatures at both locations, and found the sites to have a mean temperature difference of 0.27°C and standard deviation of 2.20°C (Fig. 2.4). The difference between the two sites shows greater variability in the fall (std = 2.64) and winter (std = 2.95) than in the spring (std = 1.44) and summer (std = 0.77), with the ice core site tending to be slightly colder (mean winter temperature difference of -0.80°C). This may be because the AWS is situated atop a nunatak. Therefore the corresponding MODIS pixel contains both snow (cooler) and rock (warmer) surfaces.

MYD21 LST data were obtained for the period 2000-2020 (https://lpdaacsvc.cr.usgs.gov/appeears/) for dates with minimal cloud cover and a viewing angle < 30°, to mitigate the effect of viewing angle on temperature and emissivity. The surface temperatures were then plotted against the MOD11 dataset covering 2000-2017 (McConnell 2019) to check for consistency. ASTER kinetic temperature data

11
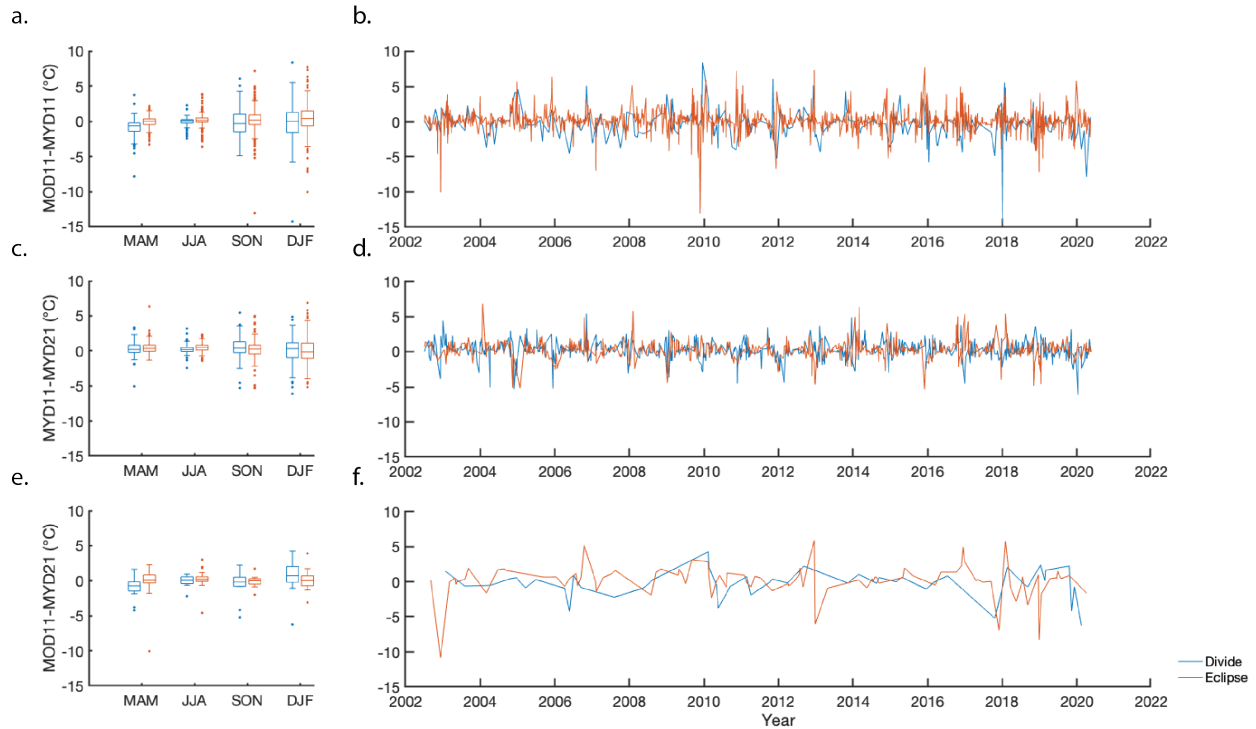
Figure 2.3. Differences between remote sensing LST products MOD11 and MYD11 (a,b), MYD11 and MYD21 (c,d), and MOD11 and MYD21 (e,f) at Divide and Eclipse. All three LST products show similar values, with the greatest variability among them in fall and winter months.

(AST08, https://search.earthdata.nasa.gov/search) for 2001-2020 were manually filtered to remove cloud cover. Four additional data values were omitted because their time of acquisition was ten hours offset from all other data points.

Finally, I examine MODIS, ASTER and Landsat brightness temperatures in addition to surface temperatures. MODIS TIR brightness temperatures (https://lpdaacsvc.cr.usgs.gov/appeears/) were extracted for the dates corresponding to the MYD21 LSTs used in this study. Digital numbers from the TIR bands of the ASTER L1T imagery (https://search.earthdata.nasa.gov/search) were converted to radiances, which were then converted to brightness temperatures using the following equations (Ndossi and Avdan 2016):
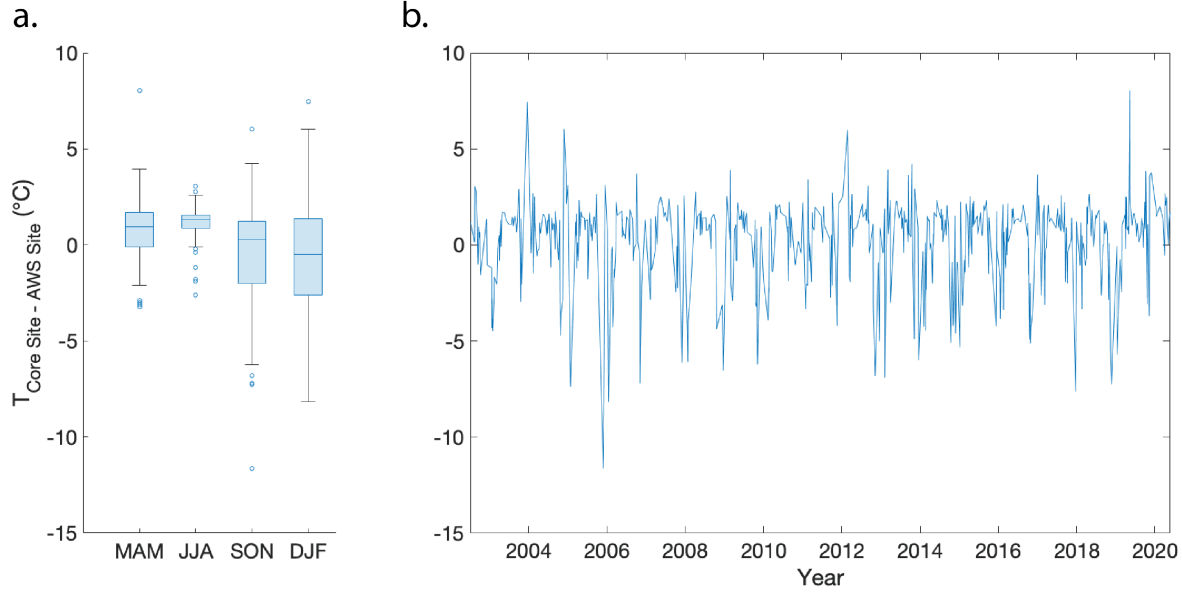
Figure 2.4. Differences between MYD21 LSTs at the Divide ice core site and Divide AWS site binned by season (a) and shown in timeseries (b). The discrepancy between the two sites is most variable in fall and winter.

Table 2.1. Unit Conversion Coefficients (UCC) of ASTER's TIR bands (Ndossi and Avdan 2016)

Band	10	11	12	13	14
UCC	0.006822	0.006780	0.006590	0.005693	0.005225

$$L_\lambda = (DN - 1) \cdot (UCC) \tag{2.1}$$

$$T_{sen} = \frac{K_2}{\ln(\frac{K_2}{L_\lambda} + 1)} \tag{2.2}$$

where L_λ is the top of atmosphere radiance in W/(m^2 sr μm), DN is the digital number of the ASTER TIR band being used, UCC is the Unit Conversion Coefficient of that TIR band (Table 2.1), T_{sen} is the top of atmosphere brightness temperature in Kelvin, and K_1 and K_2 are band-specific thermal conversion constants based on the TIR channel's operation wavelength (Table 2.2).

Table 2.2. K_1 and K_2 coefficients of ASTER's TIR bands (Ndossi and Avdan 2016)

Band	K_1 (W m^2 sr^{-1} μm^{-1})	K_2 (W m^2 sr^{-1} μm^{-1})
10	3047.47	1736.18
11	2480.93	1666.21
12	1930.80	1584.72
13	865.65	1349.82
14	649.60	1274.49

Landsat top of atmosphere brightness temperature imagery (https://earthexplorer.usgs.gov/) was manually examined for cloud cover, and appropriate pixels were extracted using QGIS. Landsat surface temperatures remain under development and were not included in this study.

2.2.2 Near-Surface Temperature Inversions

To test whether the MODIS LST cold bias reflects pervasive temperature inversions, I compare its magnitude to incoming solar radiation and wind speed measurements from the Divide AWS. Inversions result from the emission of longwave radiation from the snow surface under low levels of incoming solar radiation (Adolph, Albert, and Hall 2018). When incoming shortwave radiation is small, there is a negative energy balance at the surface, and heat is transferred from the surface to the air (Adolph, Albert, and Hall 2018). Warming of the air is required when incoming solar radiation is low for downward longwave radiation from the atmosphere to balance upward longwave radiation from the surface, as the atmosphere has a lower emissivity than the snow surface (Hudson and Brandt 2005). The effect of low solar radiation can be counterbalanced if wind speeds are high enough to disturb thermal stratification (Adolph, Albert, and Hall 2018). Therefore, I consider low wind speeds and low levels of solar radiation as prerequisites for the development of inversions, and test whether strong MODIS LST cold biases coincide with these conditions.

2.2.3   Sensor Footprint Size

To test if the cold bias is a result of the MODIS sensor's large footprint, I calculate the offsets in ASTER and Landsat surface temperatures from in situ measurements and compare them to the MODIS cold bias. ASTER is located aboard one of the satellites (Terra) that also houses the MODIS instrument, but ASTER has a smaller footprint than MODIS, their resolutions being 90 m and 1 km respectively. There is very little ASTER data available however, so I also examine Landsat data, which has a comparable spatial resolution of 100 m (LS8) to 120 m (LS4), and is available going back to 1984.

2.2.4   Snow Surface Emissivity

To test whether the MYD21 cold bias is a result of poorly constrained snow emissivity values, I assess whether the prominent wintertime cold bias in MYD21 surface temperatures is also present in MODIS brightness temperatures. Brightness temperature is a measure of an object's emitted energy assuming perfect blackbody emission and can differ considerably from the object's physical surface temperature. Emissivity is used to convert brightness temperature to surface temperature. If the cold bias were introduced prior to the brightness temperature to surface temperature conversion, we would expect brightness temperatures to exhibit a greater offset from in situ measurements in the fall and winter, similarly to the final LST product. If, however, the cold bias were introduced by the emissivity values used in this conversion, we would expect the prominent fall and winter offset to be absent from the brightness temperatures. I also examine whether greater MYD21 cold biases are associated with snowfall events in the Divide accumulation record, corresponding to snow surface evolution and emissivity changes, during and after snowfall events. Snowfall events are defined following Andin (2015), with the lower accumulation limits for high and extreme snowfall events defined as 7 and 27 cm per 12 hours, respectively.
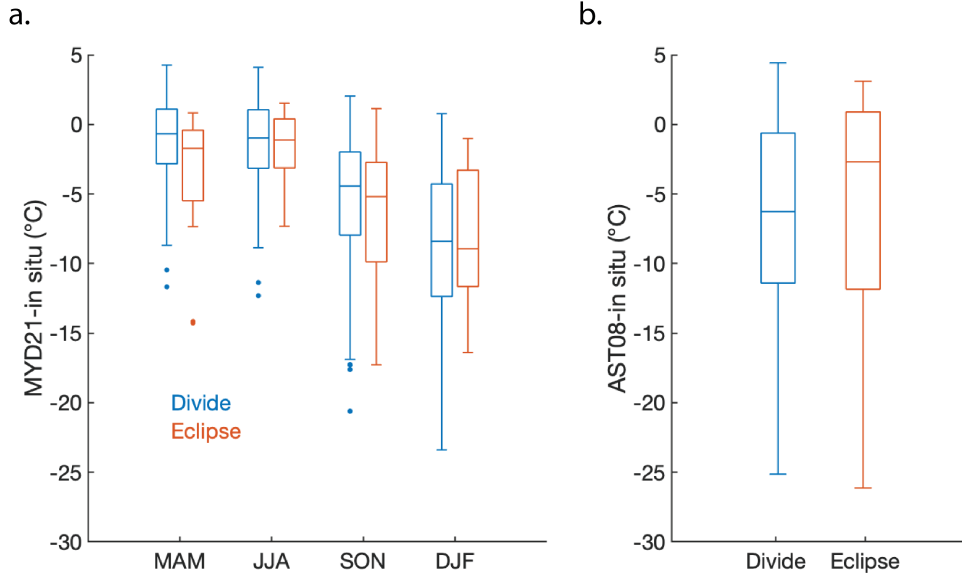
Figure 2.5. Differences between remote sensing surface temperatures and in situ measurements. Temperature products from both MODIS (a) and ASTER (b) show cold bias relative to in situ temperatures. The MYD21 cold bias is strongest in the fall and winter. ASTER did not produce enough data to bin by season.

2.3 Results

2.3.1 Near-Surface Temperature Inversions

Differences between in situ temperature measurements and MYD21 LSTs at Divide are larger in the fall (mean = -5.48°C) and winter (mean = -8.35°C) than in the spring (mean = -1.17°C) and summer (mean = -1.46°C; Fig. 2.5a). Differences between in situ temperature measurements and MYD21 LSTs at Eclipse are also larger in the fall (mean = -5.48°C) and winter (mean = -8.19°C) than in the spring (mean = -3.30°C) and summer (mean = -1.88°C). The temperature difference is most pronounced at low wind speeds and low levels of incoming solar radiation, similar to findings at Summit, Greenland (Adolph, Albert, and Hall 2018; Fig. 2.6).

2.3.2 Sensor Footprint Size

Both MODIS and ASTER surface temperatures show a cold bias relative to in situ measurements. In all seasons, the MODIS temperature difference data spans >10°C, with

16
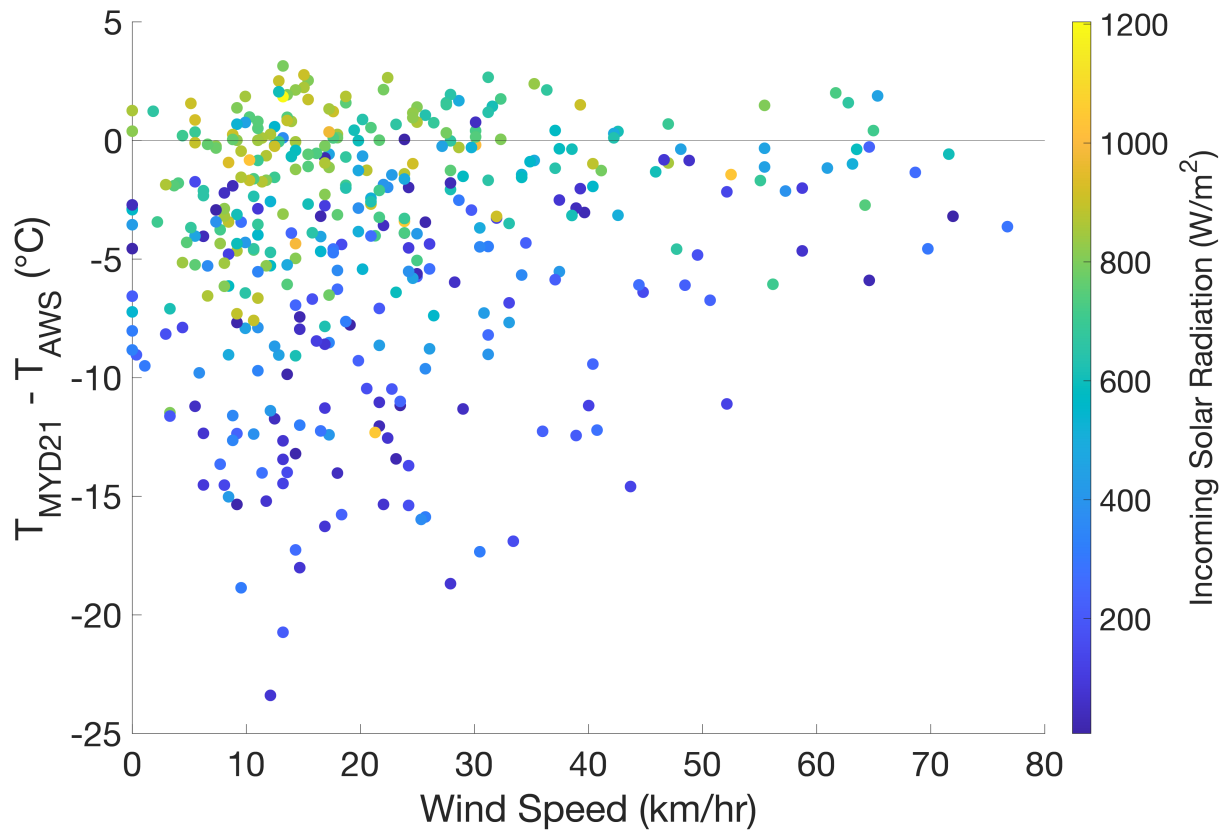
Figure 2.6. Comparison of the measured cold bias (MYD21-AWS) and measured solar radiation and wind speed. The MYD21 LSTs show the most pronounced cold bias at low levels of solar radiation (shown by marker color) and low wind speeds. Horizontal line marks all locations where MYD21 = in situ.

the range of winter values being greatest at 35.56°C (Divide) and 25.13°C (Eclipse). ASTER surface temperature data were not produced for enough dates to provide a robust dataset for each season, so the relationship between ASTER surface temperatures and in situ temperatures is examined without binning by season. On the whole, ASTER temperatures are lower than those measured in situ by a median of 6.26°C and 5.30°C, at Divide and Eclipse respectively (Fig. 2.5).
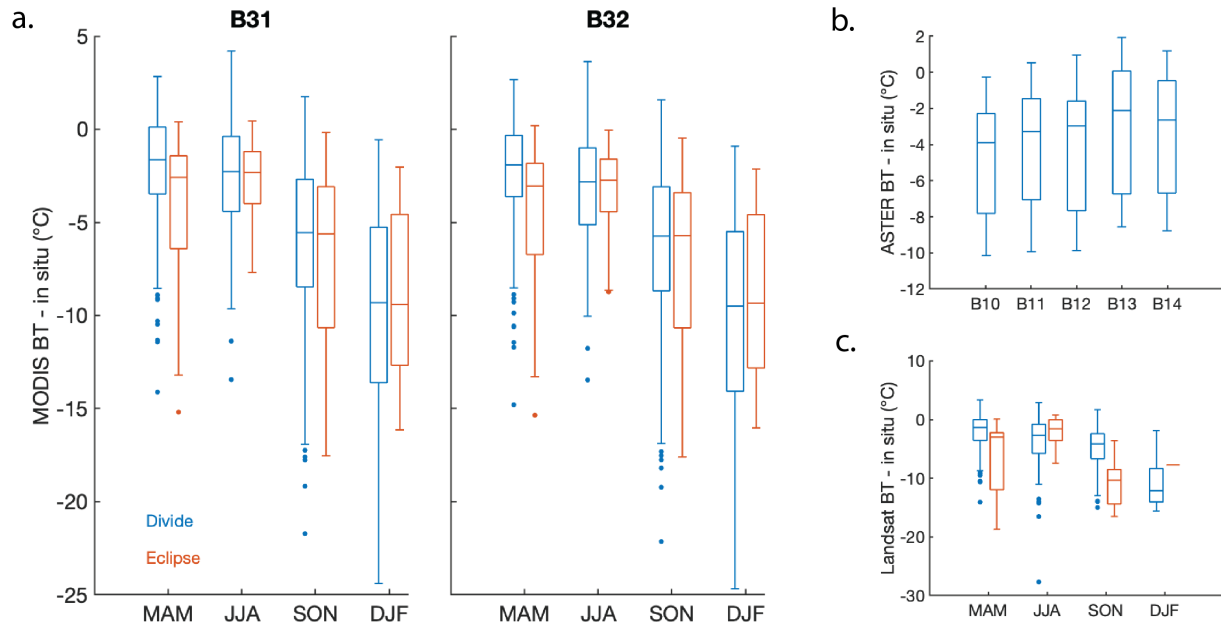
Figure 2.7. Differences between remote sensing brightness temperatures (BT) and in situ measurements. Brightness temperatures from MODIS (a), ASTER (b), and Landsat (c) show cold bias relative to in situ temperatures. MYD21 and Landsat cold biases are strongest in the fall and winter. Landsat brightness temperatures are averaged across bands from both Landsat 4-7 and Landsat 8. ASTER did not produce enough data to bin by season.

2.3.3 Snow Surface Emissivity

MODIS brightness temperatures in bands 31 and 32 (prior to the incorporation of snow emissivity) show similar cold bias patterns as the LST products (after the incorporation of snow emissivity), with the bias being most prominent in fall and winter (Fig. 2.7). Brightness temperatures for five ASTER bands (10, 11, 12, 13, 14) also show a cold bias similar to the final ASTER kinetic temperature product, although because there was not enough available ASTER data to bin by season, I was unable to compare seasonal patterns of the cold bias as with MODIS (Fig. 2.7). Like MODIS, Landsat brightness temperatures showed a greater offset from in situ temperatures in fall and winter (Fig. 2.7).

In general, the MODIS cold bias is most pronounced in the winter, which sees the highest frequency of snowfall events. However, given the temporal resolution of MODIS

18
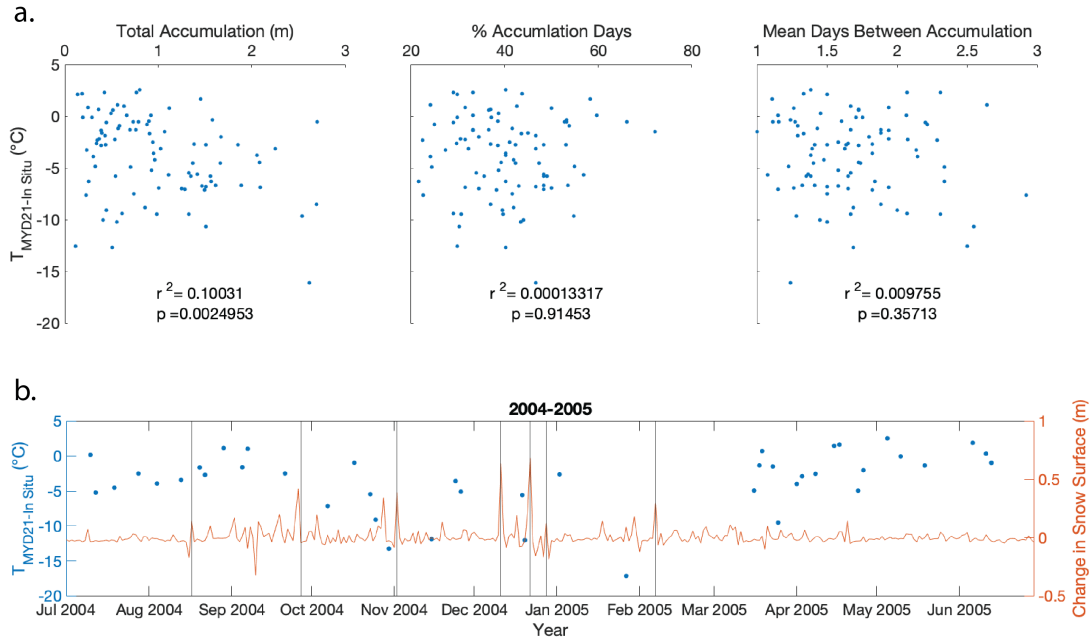
Figure 2.8. Comparison between MODIS cold bias and snow accumulation at Divide shows no correlation. Panels (a), (b), and (c) show scatterplots of monthly mean cold bias at Divide vs. total accumulation, percent of each month's days with accumulation, and mean number of days between accumulation. Panel (d) shows the cold bias and changes in snow surface at Divide for July 2004 – July 2005 (a representative year). Positive values indicate accumulation. Extreme snow events as defined by Andin (2015) are indicated by vertical lines.

data, there is no significant relationship between the cold bias and individual snowfall events. Likewise, there is no significant relationship between the cold bias and the total accumulation, the percent of days with accumulation, or the mean days between accumulation each month (Fig. 2.8).

2.4   Discussion

2.4.1   Near-Surface Temperature Inversions

The MODIS cold bias is most pronounced at low wind speeds and low levels of incoming solar radiation. Incoming solar radiation is lowest in the fall and winter and may be a root cause for the seasonal nature of the cold bias; however, low wind speeds are characteristic of summer, not winter, months (Fig. 2.9).
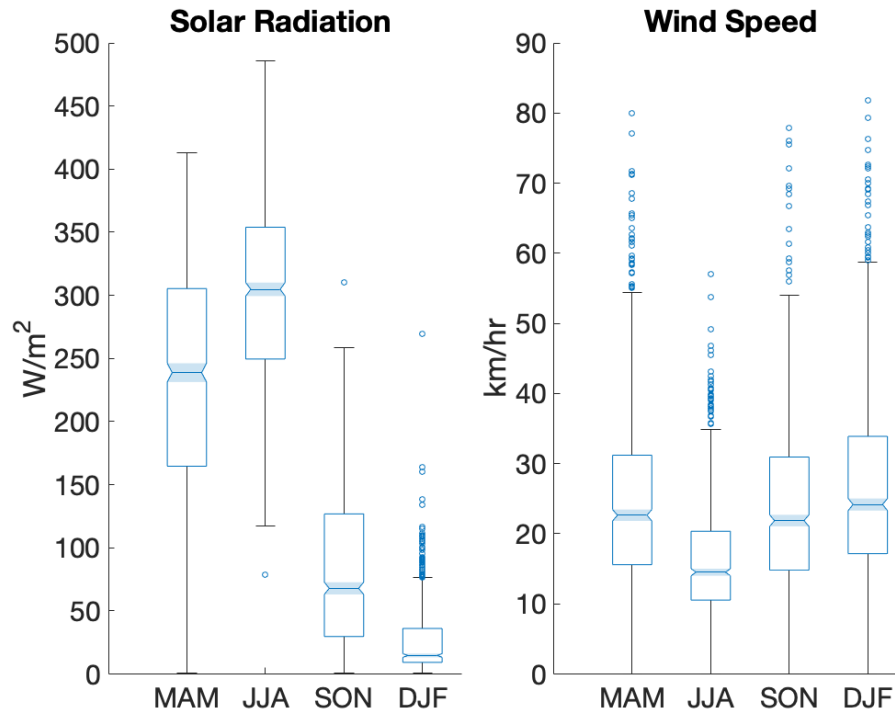
Figure 2.9. Solar radiation and wind speed by season at Divide. Notched shaded areas represent the 95% confidence interval for each season's median value. The median solar radiation values in all seasons differ significantly from one another (notches do not overlap). The median MAM wind speed does not differ significantly from the median SON or DJF wind speeds.

The cold bias is more strongly correlated with solar radiation ($r^2 = 0.34$, $p \leq 0.05$) than with wind speed ($r^2 = 0.02$, $p \leq 0.05$; Fig. 2.10). This may be because low solar radiation precipitates inversions, whereas low wind speeds simply maintain them once they exist. Inversions occur as a result of the emission of longwave radiation from the snow surface under low levels of incoming solar radiation (Adolph, Albert, and Hall 2018), which is likely what we observe here. High wind speeds disturb thermal stratification, so inversions can only be sustained under low wind conditions; however, I find that wind speed does not itself lead to inversions.
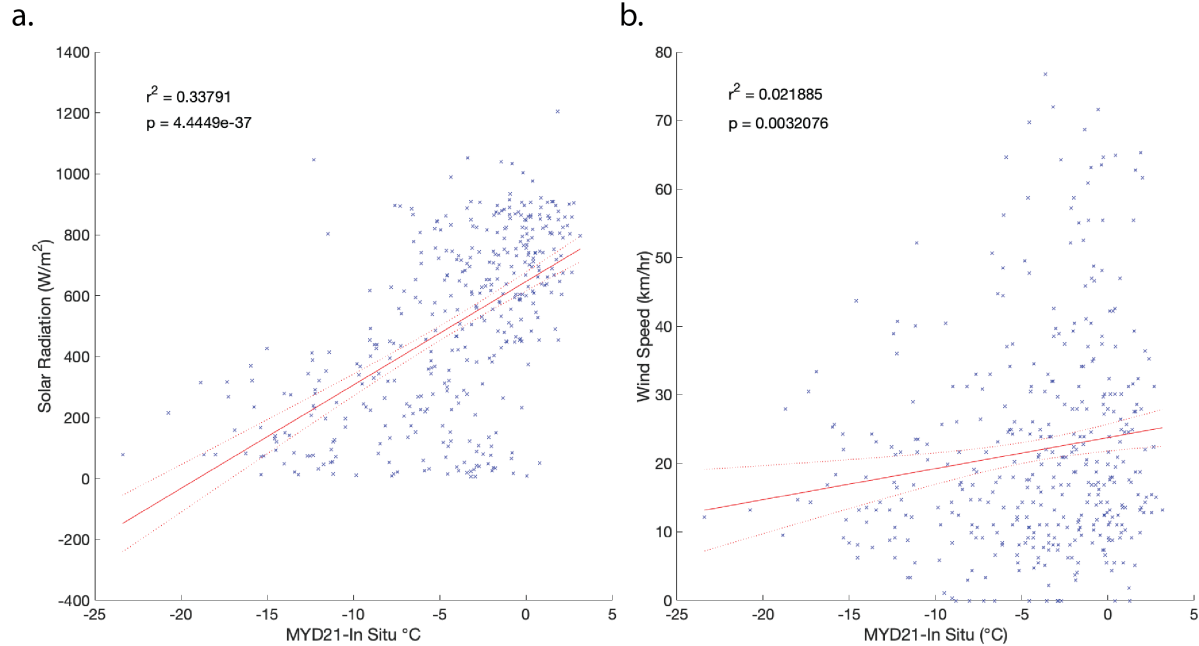
Figure 2.10. Linear regressions of the MYD21 cold bias and solar radiation (a) and wind speed (b). Solar radiation is measured in W/m^2. Wind speed is measured in km/hr. The magnitude of the MYD21 cold bias is more strongly related to solar radiation than to wind speed.

2.4.2 Sensor Footprint Size

The persistence of the cold bias in ASTER data indicates that averaging temperature over MODIS' square kilometer footprint alone does not account for the cold bias in its LSTs. ASTER surface temperatures exhibit a cold bias despite ASTER's smaller footprint and the homogeneity of surface type within the ASTER pixel relative to that within the MODIS pixel. Additionally, in situ temperatures at Divide and Eclipse show good coherence, with a mean temperature difference between the sites of 0.93°C and a standard deviation of 2.00°C, despite the two sites being 30 km apart and having over 400 m of elevation difference between them (Fig. 2.11). At its most extreme, the temperature difference measured by weather stations between the two sites reaches ∼8°C. Although 8°C is notable, the fact that it is on the upper extreme of temperature disparities over 30 km and 400 m of elevation demonstrates that averaging temperatures over a single square
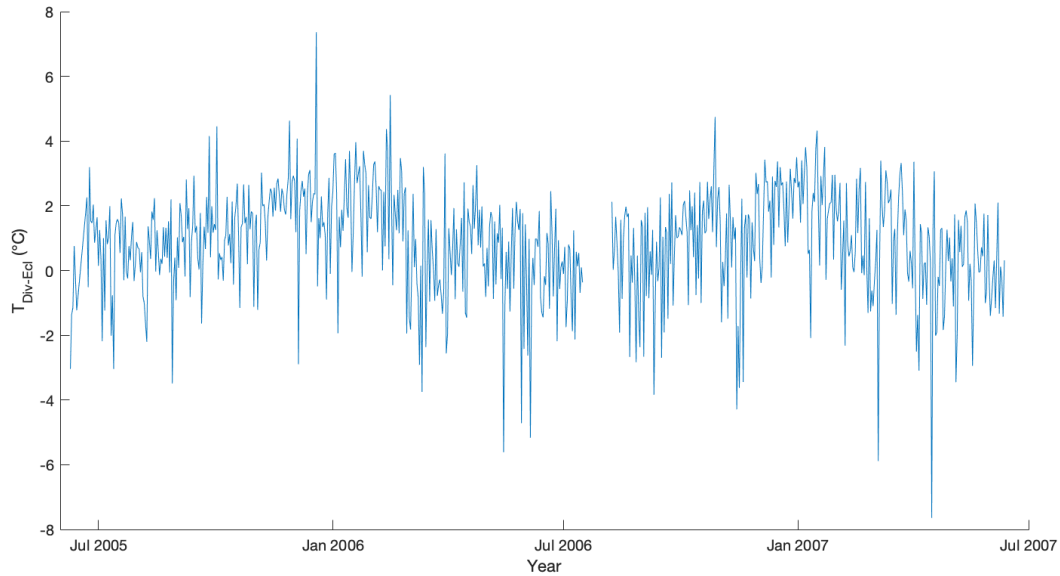
Figure 2.11. Difference between in situ air temperatures at Divide and Eclipse from July 2005-July 2007. Data missing from July 16 to August 7, 2006 due to a sensor malfunction. The two sites show good coherence in temperature, with Divide tending to be slightly warmer during the winter.

kilometer is unlikely to produce a cold bias of the magnitude observed in MODIS LSTs (over 20°C in winter conditions, Fig. 2.5).

2.4.3   Snow Surface Emissivity

Poorly constrained emissivity values also fail to account for the entire cold bias, MODIS brightness temperatures and surface temperatures show the same pattern of increased offsets from in situ measurements during the fall and winter (Fig. 2.7a). Moreover, this pattern appears in Landsat brightness temperatures as well (Fig. 2.7c).

However, emissivity cannot be ruled out as an exacerbating factor. At Divide, converting from brightness temperatures to surface temperatures brings the median offset from in situ measurements closer to zero (95% confidence interval) during spring and summer, as would be expected (Fig: 2.12). However, during fall and winter, the median offset between surface and in situ temperatures does not differ from that between
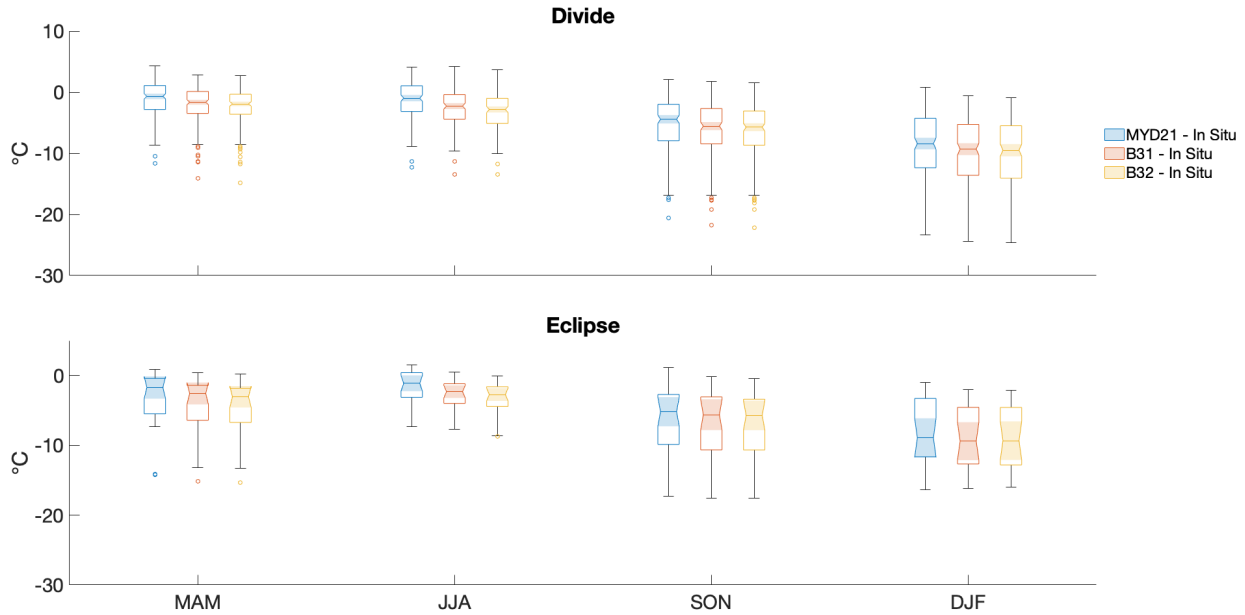
Figure 2.12. Offsets of MYD21 surface temperatures, MODIS Band 31 brightness temperatures and MODIS Band 32 brightness temperatures from in situ measurements at Divide and Eclipse. Spring and summer MODIS cold biases are smaller in the final surface temperatures than in brightness temperatures (95%confidence interval). Fall and winter MODIS cold bias show no difference between final surface temperatures and brightness temperatures (95% confidence interval).

brightness and in situ temperatures (95% confidence interval). This distinction cannot be attributed to relatively few fall and winter samples, as 169-203 MYD21 LSTs were collected for each season. At Eclipse, the median offset between surface and in situ temperatures did not differ from that between brightness and in situ temperatures in any season (95% confidence interval) due to the much smaller sample size (20-30 data points per season). Emissivity values may be especially poorly known under winter conditions because of rapidly changing snow surface characteristics, resulting in the seasonal difference in outcome of the LST algorithm as seen at Divide. In particular, the role of emissivity changes following snowfall events requires further examination. Emissivity increases with surface melt, and decreases with increasing particle size and density, which can occur due to either packing or welding of grains as the snow surface evolves following a snowfall event

23

(Salisbury, D'Aria, and Wald 1994). Without field measurements, I could not directly observe the snow surface evolution after snowfall, and the surface could evolve in any number of ways during a given period depending on the combination of environmental factors at play. Changing temperatures could cause melt and/or refreezing over hours; shallow layers of refrozen melt in an ice core taken at Mt. Hunter (Alaska) have been paired with above-freezing temperatures on specific days (Winski et al. 2018). Likewise, intense wind could rapidly change the surface quality of a particular location by scouring or depositing snow. Given that temperature and wind speed can interact in any number of ways with each other and with local topography, it's unsurprising that temporal patterns of snow accumulation in themselves do little to predict the presence or magnitude of a cold bias. At present, I limit myself to this cursory examination of emissivity in relation to the Divide accumulation record because my focus is on summer processes, when ablation rather than accumulation dominates. I focus on summer processes because of the importance of summer temperature for glacier melt and mass balance. In order to examine the relationship between snow surface evolution and emissivity in more detail, I suggest pairing in situ measurements of emissivity and surface characteristics at sub-daily resolution.

2.4.4   MODIS Cloud Masking and Blowing Snow

Clouds and blowing snow may also produce low LSTs if they are erroneously categorized as the land surface. MODIS employs a cloud-masking technique to determine whether the required clear-sky conditions are available for temperature production; however, imperfect cloud masking can lead to the inclusion of cold cloud-top conditions averaged into the LST (Westermann, Langer, and Boike 2012). Summertime cold biases in MODIS surface temperatures ($\sim3°C$) at Summit, Greenland have been attributed to errors in cloud masking (Koenig and Hall 2010). Similarly, wintertime MODIS cold biases ($\sim5°C$) at Summit have been attributed to a combination of reduced accuracy in cloud masking during the polar night and increased solar zenith angle (Shuman et al. 2014).

2.4.5 MODIS LSTs and Melt

Despite lingering uncertainty about the source of their cold bias, and the lack of an accurate correction, MODIS LSTs can still shed light on the important question of surface melt and mass balance in the North Pacific. The cold bias is most prominent in the fall and winter (mean = -8.35, std = 4.95); during the summer the cold bias is relatively minor (mean = -1.46, std = 3.11). Surface melt is largely driven by high air temperatures, which tend to occur under cloudy conditions (Walsh and Chapman 1998). This preferentially precludes the production of MODIS LSTs on high-melt days and renders them ineffective for examining individual extreme melt events. However, interannual trends in MODIS LSTs (MOD11, MYD11, and MYD21) agree well with those in situ temperatures (Fig. 2.13). MODIS LSTs can therefore be used to at least qualitatively inform our interpretation of refrozen melt layers in ice cores, which can provide information about past summer temperature conditions. In chapter 3, I discuss melt layers in an ice core taken at Eclipse in 2016, and their potential interpretation as a summer temperature proxy.

2.5 Conclusions

I found that the physical conditions (low wind speeds, low levels of incoming solar radiation) associated with greater MODIS cold biases are consistent with those associated with near-surface temperature inversions over Greenland. The MODIS cold bias may therefore be representative, at least in part, of a physical process affecting the relationship between the two slightly different properties measured by MODIS (skin temperature) and weather stations (air temperature) rather than the instrumentation or algorithm used to calculate LSTs.

I also found that neither the MODIS sensor's large footprint size nor poorly constrained emissivity values account for the cold bias in MODIS LSTs relative to in situ temperature measurements. Even in highly heterogeneous alpine terrain, the spatial coherence of temperatures across study sites in the region makes it doubtful that offsets from in situ

Figure 2.13. Mean annual MODIS and in situ temperatures at Divide. Results show a prominent cold bias in the remote sensing measurements (purple, yellow, orange lines) compared to the in situ measurement (blue line), but overall agreement in years of high vs. low temperatures.

temperatures in excess of 10°C could be regularly obtained by averaging temperatures across a single square kilometer to produce the MODIS LST. Moreover, surface temperatures from the ASTER sensor, which has a footprint of 90 m as compared to MODIS' 1 km, still exhibit a cold bias relative to in situ measurements. Correcting for the MODIS LST cold bias will therefore require efforts beyond simply improving the spatial resolution of remote sensing data.

Correcting for the MODIS LST cold bias will also require efforts beyond narrowing the constraints on emissivity values used to calculate the LSTs; the pattern of greater offset from in situ temperatures is present in MODIS data even prior to the incorporation of snow surface emissivity. Despite the fact that the cold bias does not originate from the incorporation of emissivity, poorly constrained emissivity values could exacerbate a cold bias already present, particularly after snowfall events, when emissivity is likely to change rapidly due to settling and compaction processes. The MODIS cold bias is more

26

pronounced in the winter, when more snowfall events occur; however, higher temporal resolution is needed on the MODIS data to examine the response of the cold bias to individual snowfall events. In short, emissivity values are not responsible for the production of the MODIS cold bias, but their role in amplifying the bias remains unknown.

Regardless of the source of the cold bias, MODIS LSTs are in good agreement with in situ temperature measurements throughout the summer melt season. Consequently, they do provide reliable information on summer temperatures in the St. Elias beyond the limited in situ record and can be used to examine the relationship between summertime warming and ablation in the region.

CHAPTER 3

MELT LAYERS IN THE 2016 ECLIPSE ICE CORE

3.1 Background and Goal

Layers of refrozen melt in ice cores form when surface melt percolates down through the snowpack before refreezing at the 0°C isotherm (Pfeffer and Humphrey 1998). The amount of melt produced at the surface is controlled by the net surface energy balance (E_N), which can be expressed by:

$$E_N = E_S + E_L + E_G + E_H + E_E + E_P \tag{3.1}$$

where E_S is the net shortwave radiation, E_L is the net longwave radiation, E_G is the subsurface energy flux, E_H and E_E are the turbulent sensible and latent heat fluxes, and E_P is the heat flux associated with liquid precipitation that subsequently freezes (Cuffey and Paterson 2010). Assuming a surface layer thick enough to eliminate the effect of seasonal temperature variations at its bottom, subsurface energy flux can be approximated as $E_G \approx 0$. I also ignore E_P at Eclipse, as rainfall is a relatively unimportant process in the St. Elias icefields, leaving:

$$E_N = E_S + E_L + E_H + E_E \tag{3.2}$$

A positive E_N will drive melt if the surface has warmed to the melting point, whereas a negative E_N will drive freezing of any available liquid water (Cuffey and Paterson 2010). E_N will increase with the increase of any one of its four components. In effect, increases in E_N (and melt production) are largely driven by three factors: increases of net shortwave radiation, increases of downward longwave radiation, and increases of sensible heat transfer (Cuffey and Paterson 2010). Upward longwave radiation ceases to be important once the surface starts to melt; at this point, its temperature, and consequently its upward longwave radiation, cannot increase further. Both downward longwave radiation and sensible heat

28

transfer increase with atmospheric temperature, making atmospheric warming a key driver of surface melt production (Cuffey and Paterson 2010).

Because of the direct physical link between high surface temperatures and surface melt, ice core melt layers can be related back to surface conditions at their time of production. This is done by measuring the water contained in each layer and calculating the energy required to produce it. Despite their robustness as a summer temperature proxy, very few melt records exist and their spatial distribution is largely restricted to the eastern Arctic (e.g. Graeter et al. 2018; Kinnard et al. 2011; Trusel et al. 2018; Zdanowicz et al. 2012). Melt layers therefore present an opportunity to expand our paleoclimate understanding and complement existing records of other types. For example, the processes of melt production and percolation are influenced by different environmental factors (e.g. wind speed, surface roughness) than those that influence isotope fractionation (e.g. temperature gradients, moisture transport path), another commonly used temperature proxy. Deriving temperature from both proxies where possible will thus provide a more nuanced picture of past climatic conditions.

Although surface energy balance is affected by a number of factors (wind speed, humidity, cloud cover, snowfall, surface characteristics), surface temperature is the primary determinant of melt production, and surface temperature as quantified by positive degree days (PDDs) has been shown to correlate well with ice ablation (Cuffey and Paterson 2010; Braithwaite 1995). However, local influences on melt production can be significant. The relationship between melt and temperature must therefore be examined at any given site before melt layers can be confidently used to reconstruct past temperatures.

Additionally, an intact melt record requires that all melt produced in a year remains trapped in that year's stratigraphic layer, but with sufficiently high and sustained surface temperatures, melt can percolate into prior years' snowpack. In a series of experiments conducted at Siple Dome, a PDD value of 5.22 was found sufficient to produce melt layers below the present year's accumulation, while a PDD value of 1.57 was not (Das and Alley

29

2005). If surface melt percolates into a subsurface layer that is below the freezing temperature, it will partially refreeze, releasing latent heat and warming the snowpack. Once the entire snowpack has been warmed to the melting point, melt will no longer refreeze and instead continue to percolate further down into the firn column (Benn and Evans 2010). Most of the energy that warms the snowpack is supplied by latent heat associated with refreezing melt rather than the diffusion of heat downward from the surface (Cuffey and Paterson 2010).

The goal of this chapter is to determine whether melt layers in the Eclipse ice core record are representative of summer temperature conditions on the icefield. To achieve this goal, I address the following questions:

1. Do Eclipse ice core layers containing abundant refrozen melt coincide with years of high summer temperatures?

2. Does surface melt at Eclipse provide sufficient latent heat to raise the current year's snowpack temperature to 0°C and enable percolation into prior years?

3.2   Methods

3.2.1   Study Sites

Eclipse Icefield (60.84°N, 139.84°W) is located at an elevation of 3,017 m a.s.l in the Upper-Kaskawulsh Donjek region of the St. Elias Range (Fig. 1.1). A firn core was drilled to a depth of 58.96 m at Eclipse in 2016 (McConnell 2019). A second core was drilled to a depth of 18.60 m the following year (McConnell 2019). Age-depth scales for each core were derived using glaciochemical signals to delineate annual layers (McConnell 2019). Four independent researchers (E. McConnell, K. Kreutz, D. Winski, W. Kochtitzky) used δ^{18}O, δD and deuterium excess to pick the approximate position of January 1st for each layer; the four positions were then reconciled for a final timescale (McConnell 2019). Ground-Penetrating Radar (GPR) profiles were also collected at Eclipse in both 2016 and

2017. Finally, a Maxim Integrated iButton Data Logger DS1922L ($\pm$ 0.5°C) was installed in 2016 and retrieved the following year (McConnell 2019). In addition to the iButton, an AWS was in operation at Eclipse from 2005-2007. Sensor specifications are described above in section 2.2. Icefield Divide (60.68°N, 139.78°W, 2,603 m a.s.l) is located approximately 30 km from Eclipse (Fig. 1.1). An AWS is maintained at Divide by the University of Ottawa (sensor specifications in section 2.2).

3.2.2 Temperature Datasets

To obtain a temperature record with maximum temporal coverage, I use both in situ temperature records and MODIS LST data. In situ temperatures were obtained from the AWS at Eclipse and Divide, and from the iButton at Eclipse. Sensor specifications are described in section 2.2.

I use three MODIS LST products: MOD11, MYD11 and MYD21. Product specifications are described in section 2.2. Although the MxD21 products superseded MxD11 products in 2017, I include both generations of MODIS LSTs in this study. As discussed in section 2.2, both products show good agreement, especially during summer months (Fig. 2.3). However, MxD21 products employ stricter cloud detection standards than their MxD11 counterparts, and thus produce LSTs for fewer dates. All MODIS LST data (https://lpdaacsvc.cr.usgs.gov/appeears/) were obtained for dates with minimal cloud cover and a viewing angle < 30°, to mitigate the effect of viewing angle on temperature and emissivity. The time periods covered by all datasets used in this study are shown in Figure 1.2.

3.2.3 Positive Degree Days

Mean summer temperatures and PDDs per year were calculated for each temperature dataset. Annual PDD values approximate the energy driving melt each year, and correlate with mean summer temperatures whether using MODIS (r^2 values from 0.21 to 0.57) or in situ data ($r^2 = 0.95$; Fig. 3.1). However, even after scaling by the number of observations
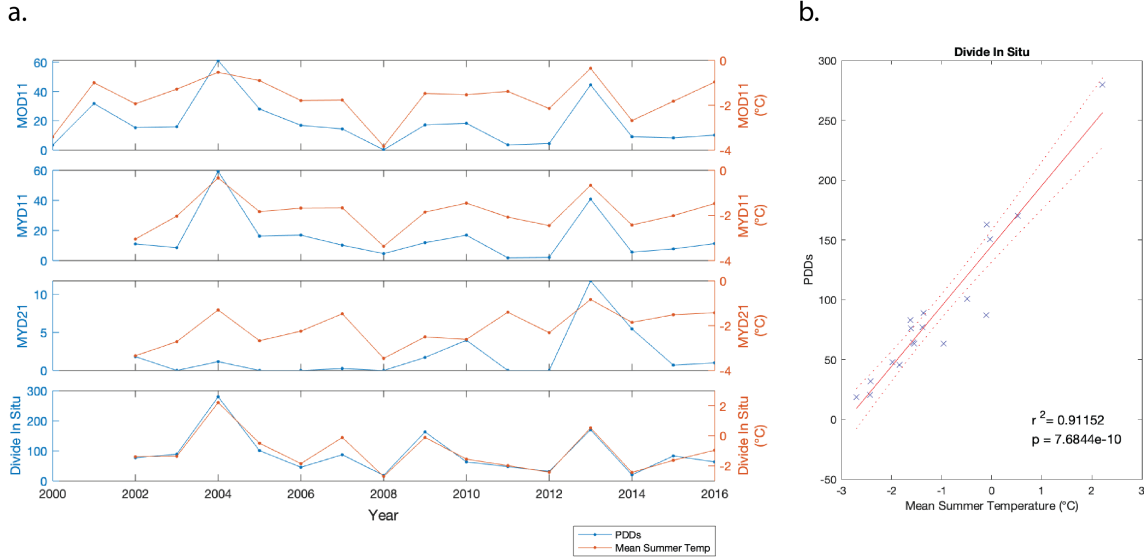
Figure 3.1. Positive degree days and mean summer temperatures in the Upper Kaskawulsh-Donjek region. A) PDDs and mean summer temperatures are calculated from MOD11 LSTs at Eclipse, MYD11 LSTs at Eclipse, MYD21 LSTs at Eclipse, and AWS temperatures at Divide. In situ temperatures at Eclipse are not used due to lack of data. B) PDDs show high correlation with mean summer temperatures calculated from in situ temperature measurements.

per year, annual PDD values calculated from MODIS LSTs are notably smaller than those calculated from in situ temperatures. This is because MODIS LSTs were not produced on many of the days when high ($>2°C$) in situ temperatures were recorded, likely due to cloud cover (Fig. 3.2). This inhibits the use of absolute PDD values in my analysis, but interannual trends in the PDD data remain informative. I therefore compare the Eclipse melt record with each set of PDDs, which have been normalized to examine interannual trends rather than absolute PDD values.

3.2.4   Eclipse Ice Core Melt

Melt layers in the Eclipse ice core were manually identified and then quantified using two metrics (thickness and intensity) following Winski et al. (2018). Melt layers appear as dark (low brightness) bands of ice as a result of their low bubble density relative to the surrounding matrix. Layer intensity is defined as the maximum magnitude of the layer's
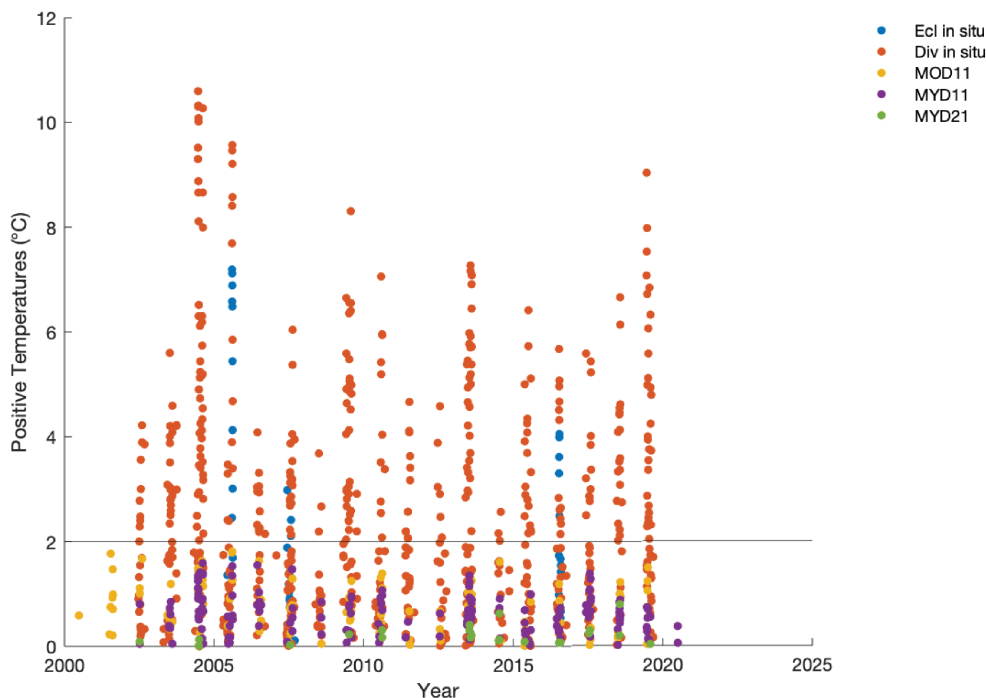
Figure 3.2. Positive temperatures from MODIS and AWS measurements. All MODIS LSTs are from Eclipse. In situ temperatures from Divide and Eclipse are shown. A horizontal line at 2°C marks the approximate upper limit of MODIS LSTs produced.

brightness anomaly relative to the surrounding matrix (Winski et al. 2018). Layer edges, background intensity, and the width of the swath over which intensity was calculated were varied for a total of 12 different intensity calculations for each melt layer. The median of these results was used in our analyses here. The median intensity value for each layer was corrected for a bias toward higher intensities in the snow and firn than in the ice, and melt layers were calibrated to a spectrum of 0 to 1 relative to the density of the surrounding matrix. Finally, layer thicknesses were adjusted to account for thinning at depth. Layers were adjusted to their thickness at the time of formation at the surface, and any layer that would have thinned to <1 mm at the bottom of the record was excluded to account for layers that would be undetectable after advection down core.

3.2.5   Divide Ablation

I calculate surface ablation at Divide using snow sounder measurements from the Divide AWS (2003-2012). Twice daily readings of snow surface height (distance to sensor) were taken using a Campbell SR50 sensor. Snow surface heights were adjusted to account for changes in the mast height of the sensor and manually filtered to remove erroneous measurements (e.g. broken mast, sensor malfunction or burial). I calculate the total melt season ablation each year by summing all decreases in snow surface height over the summer months (JJA).

3.2.6   Energy Balance Calculations

To calculate the energy supplied by meltwater-associated latent heat at Eclipse, I estimate total summer melt based on a snow accumulation record from nearby Divide. I assume that total summer melt at Divide is comparable to that at Eclipse, which is 30 km to the south-southeast, and approximately 400 m higher in elevation. To account for compaction processes causing some surface lowering, I exclude data from each accumulation event and the two days following. Following Cuffey and Paterson (2010), I assume that compaction becomes negligible relative to melt after this two-day period. I also assume that wind scour and deposition are negligible relative to melt. More work is necessary to quantify the effect of wind scour on the snow surface at these sites; however, the record of melt in recovered ice cores at Eclipse and the snowpack wetness at Divide indicate that melt is a dominant process at both locations. Additionally, given the similarity in temperature at both sites (Fig. 2.11), it is reasonable to assume that the total summer melt production is similar at Divide and Eclipse although liquid storage conditions may differ.

To calculate the total melt required to percolate through one year's snowpack at Eclipse, I compute the heat transfer required to bring one year's worth of accumulation from its mean annual temperature to the 0°C (as the snowpack must reach the freezing point to allow the coexistence of snow and liquid water), and then calculate the amount of

refreezing melt required to supply the necessary latent heat. The heat (q) required to raise the snowpack temperature and that associated with the refreezing of melt are given by Equations 3.3 and 3.4 respectively:

$$q = m_{snow} c \Delta T \qquad (3.3)$$

$$q = m_{melt} L_f \qquad (3.4)$$

where m_{snow} is the mass of one year's snowpack (kg), c is the specific heat of snow (kJ kg^{-1} K^{-1}), ΔT is the difference between 0°C and the snowpack's mean annual temperature, m_{melt} is the mass of refreezing melt (kg), and L_f is the latent heat of freezing of water (kJ kg^{-1}). Setting these two expressions for q equal, I obtain:

$$SAc(0 - \overline{T}) = Sd\rho_{water} L_f \qquad (3.5)$$

which simplifies to

$$A\rho_{snow} c(0 - \overline{T}) = d\rho_{water} L_f \qquad (3.6)$$

where S is surface area (m^2), A is annual accumulation (mm w.e. or kg m^{-2}), ρ_{snow} and ρ_{water} are the density of snow and water respectively (kg m^3), $\overline{T}$ is the mean annual temperature of the snowpack (K), and d is the depth or thickness of melt (m). I use McConnell et al.'s annual accumulation rate of 1.4 m w.e. at Eclipse, and run two sets of calculations with two different snowpack temperatures: -15.96°C under the assumption that the mean annual snowpack temperature is approximately the same as the mean annual air temperature, and -8.502°C under the assumption that the top of borehole temperature measured at the Eclipse ice core site is representative of the mean annual snowpack temperature. I assume the specific heat of snow to be the same as that of ice at a given temperature, as the heat requirement for warming the air and vapor in snow pores is very small (Mellor 1977). Here, I use 1.980 kJ kg^{-1} K^{-1} and 2.027 kJ kg^{-1} K^{-1} for the -15.96°C and -8.502°C snowpack scenarios respectively (Giauque and Stout 1936).

3.2.7 Melt Percolation Model

To further assess the likelihood of interannual melt percolation at Eclipse, I employ Meyer and Hewitt's melt percolation model to examine the evolution of snowpack temperature and saturation over time (Meyer and Hewitt 2017). The model consists of conservation of mass (ice and water) and Darcy's Law for fluid flow through a porous medium. Compaction is parametrized and kinematic and surface energy balance boundary conditions are set. The model is forced with a prescribed surface energy flux, and annual accumulation and liquid precipitation rates. Outputs include temperature, porosity and saturation profiles over time. For a full description of the model, see Meyer and Hewitt (2017). Following Meyer and Hewitt (2017), I calculate the forcing energy flux, $Q(t)$, using meteorological data at Divide, and then use the long-term mean and amplitude of variability to prescribe a sinusoidal energy flux of the form:

$$Q(t) = \overline{Q} - Q_0 \cos(\frac{2\pi t}{t_0}) \tag{3.7}$$

My energy flux calculations are detailed in Appendix B. In my prescribed flux, I use a $\overline{Q}$ value of -84.53 W m^{-2} and a t_0 value of 1 year. I prescribe an annual accumulation rate of 1.4 m w.e. a^{-1} and an annual rainfall of 0 m w.e. a^{-1}, since no rainfall has been observed at Eclipse. In addition to modeling melt percolation in response to average conditions at Eclipse, I do the same at Divide, using an accumulation rate $a = 1.6$ m w.e. a^{-1}. The amplitude of variability in my calculated surface energy values ranges from approximately 130 W m^{-2} to 160 W m^{-2}. To select the appropriate amplitude for my prescribed sinusoidal energy flux, I run the model for both Eclipse and Divide using Q_0 values from 130 to 160 W m^{-2} at intervals of five. A Q_0 value of 145 W m^{-2} most accurately replicates observed differences between the two sites and is used in all subsequent simulations.

Using a Q_0 value of 145 W m^{-2}, I force the model with the annual accumulation rate at Eclipse ($a = 1.4$ m w.e. a^{-1}) and mean annual surface energy fluxes from 2014 (-86.81 W m^{-2}) and 2016 (-79.81 W m^{-2}). 2014 (2016) was chosen because of its low (high) mean

summer temperatures and PDDs; these two scenarios represent modern end-member melt season conditions at Eclipse. In all simulations, the model was run for 100 years to allow steady state conditions to be reached.

3.2.8 Ground-Penetrating radar

GPR profiles were collected at both Divide and Eclipse to observe snow stratigraphy and water content. High-resolution profiles were collected of the upper 20-30 m of firn at Eclipse and Divide in 2016 and 2018 respectively (McConnell 2019). Profiles were collected using a Geophysical Survey Systems Inc. (GSSI) SIR-3000 control unit coupled with a model 5103 400 MHz bistatic antenna unit. The antenna was towed by hand at a speed of approximately 0.3-0.5 m/s and polarized orthogonally to the profile direction. Two-way travel time for the profile traces was 250-300 ns. 2,048 samples were obtained per scan, with 24 scans per second. Range gain was used in recording the GPR profiles to accommodate for attenuation. Additional low-resolution GPR profiles were collected using Blue System Integration's IceRadar system with 10 MHz and 5 MHz antenna units at Eclipse (2016) and Divide (2018) respectively.

3.3   Results

3.3.1   Energy Balance and Melt Production

I find that years with high PDDs do not coincide with those containing high melt in the Eclipse core (Fig. 3.3). Years of high melt are offset from those with high PDDs, and variability in PDDs fails to explain variability in melt ($r^2 \leq 0.15$, $p \geq 0.05$, Fig. 3.3a-d). Additionally, during most years, the melt produced at Eclipse was enough to warm the entire year's snowpack to the melting point and percolate through to the previous year (Fig. 3.3g). Using my more conservative estimate of snowpack temperature (-15.96°C), out of the ten years from 2003-2012, only three (2007, 2010 and 2012) lacked sufficient melt to

percolate through to the previous year. Using a snowpack temperature of -8.502°C, only 2007 and 2010 lacked sufficient melt to percolate through to the previous year.

3.3.2   Melt Percolation Model

Using Meyer and Hewitt's model, I find that under mean conditions at Eclipse, the top several meters of the firn column undergo seasonal fluctuations in porosity, saturation, and temperature (Fig. 3.4). In the summer, the near-surface porosity decreases, while saturation and temperature increase. Porosity approaches zero within the first six meters of the surface, where a band of saturated firn sits atop an impermeable layer below. A warming front raises the snow temperature up to 0°C to 6-8 meters depth in the summer, but temperatures beneath this remain below the freezing point year round.

When comparing end-member temperature scenarios at Eclipse, 2014 (cold) conditions show the least surface ablation, while 2016 (warm) conditions show the most (Fig. 3.5). In contrast, 2014 conditions show the deepest penetration of a warming front (0°C exceeding 10 m depth) despite having the lower mean annual temperature and surface energy flux. The seasonal warming front under 2016 conditions reaches only approximately 5 m in depth.

3.3.3   Ground-Penetrating Radar

GPR profiles from Eclipse and Divide show clear stratigraphic differences. In particular, the deep (10 MHz, surface to bedrock) profile from Divide shows a layer of enhanced reflectance at approximately 25 m in depth (McConnell 2019). A similar feature in a radar profile from Upper Yentna Glacier (Alaska) has been interpreted as evidence of a liquid water table formed from percolating melt (Campbell et al. 2012). No such feature appears in the Eclipse profile (McConnell 2019). Shallow (400 MHz, upper 20-30 m) profiles also show greater radar signal attenuation at Divide than Eclipse, indicative of a wetter subsurface environment (McConnell 2019).
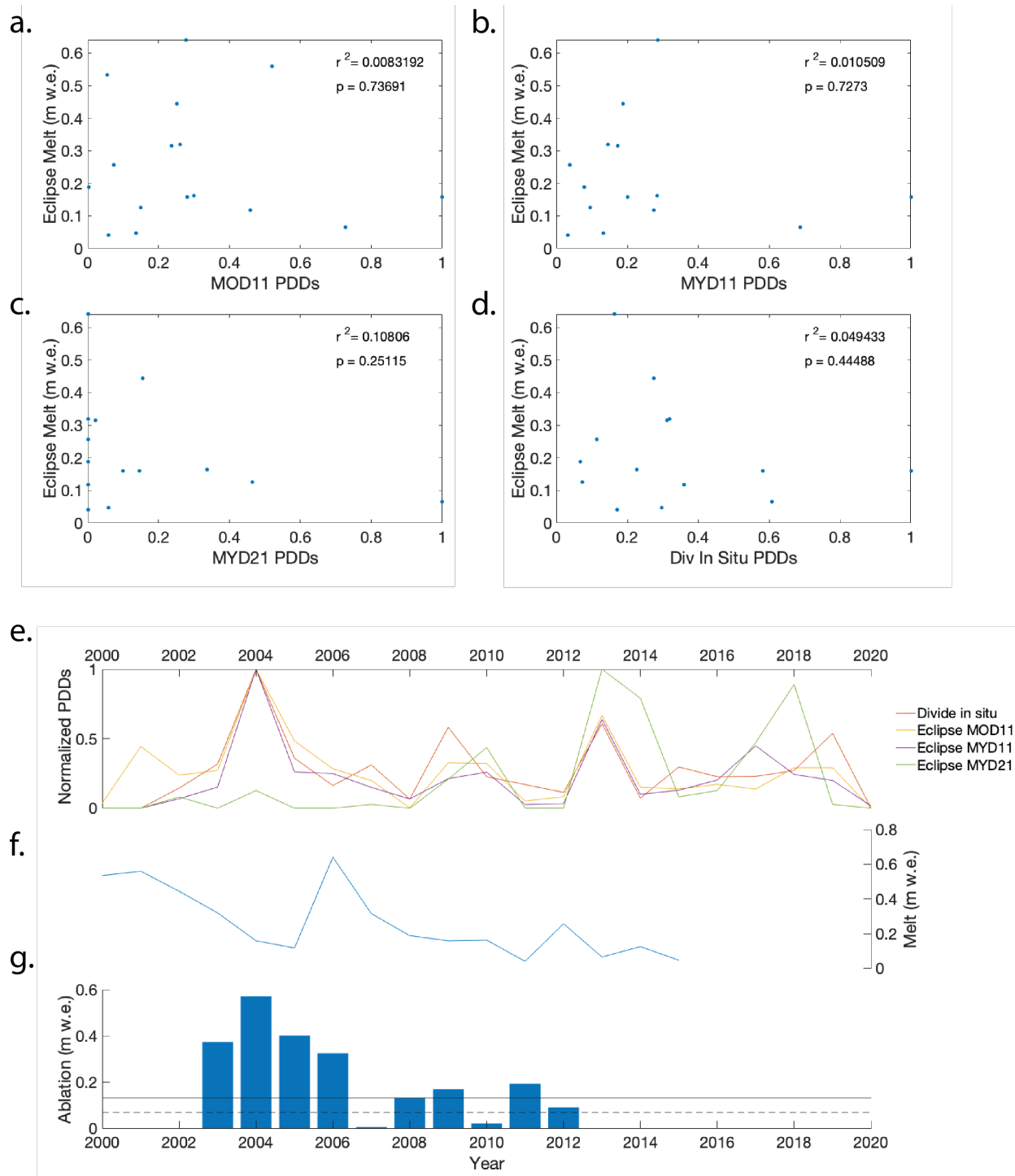
Figure 3.3. Eclipse melt record is offset from Divide ablation and annual PDDs. Scatterplots are shown of Eclipse melt and PDDs as calculated from MOD11 LSTs (a), MYD11 LSTs (b), MYD21 LSTs (c), and in situ temperatures at Divide (d). Timeseries are shown of each set of PDDs (e), Eclipse melt (f), and Divide ablation (g). The minimum melt required to warm one year's snowpack from -15.96°C to 0°C is shown by the solid horizontal line in panel (g). The minimum melt required to warm one year's snowpack from -8.502°C to 0°C is shown by the dashed horizontal line.

39
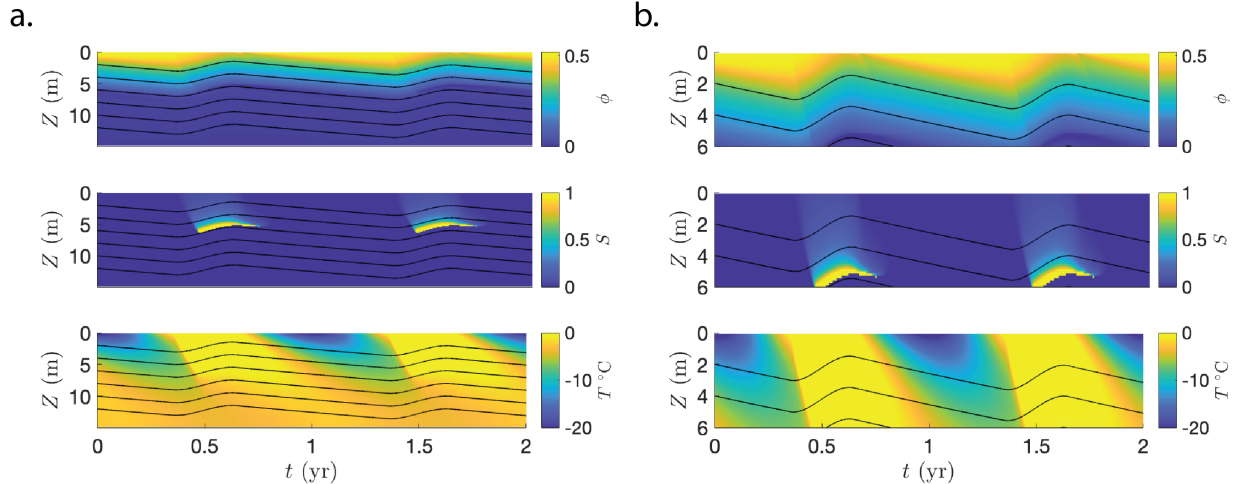
Figure 3.4. Space-time diagrams showing the evolution of porosity, saturation, and temperature as a function of time over the top 15 m (a) and top 6 m (b) of the Eclipse firn column. The model was forced with an accumulation rate of $a = 1.4$ m w.e. a^{-1} and a mean annual surface energy forcing of $\overline{Q} = -84.53$ W m^{-2}. Seasonal saturation and warming fronts penetrate the top $\sim$6 m of high-porosity surface layers.

3.4   Discussion

3.4.1   Energy Balance and Melt Production

The offset of high temperatures from high melt in the Eclipse core suggests that melt production is sensitive to local site or surface conditions other than temperature, or that melt is percolating into previous years' snowpack and distorting the record. Although melt production is most directly tied to high temperatures, other factors such as wind speed, humidity, cloud cover, snowfall, and surface conditions affect the surface energy balance and melt production (Cuffey and Paterson 2010). However, PDDs have been shown to be a better predictor of melt production than would be expected, given the complexity of the physics, and temperatures have been shown to correlate well with melt production at numerous sites with varying surface and meteorological conditions (e.g. Braithwaite 1995; Kelsey et al. 2010; Trusel et al. 2018; Winski et al. 2018). In addition, years with high PDD values are coincident with high ablation at Divide (Fig. 3.3).
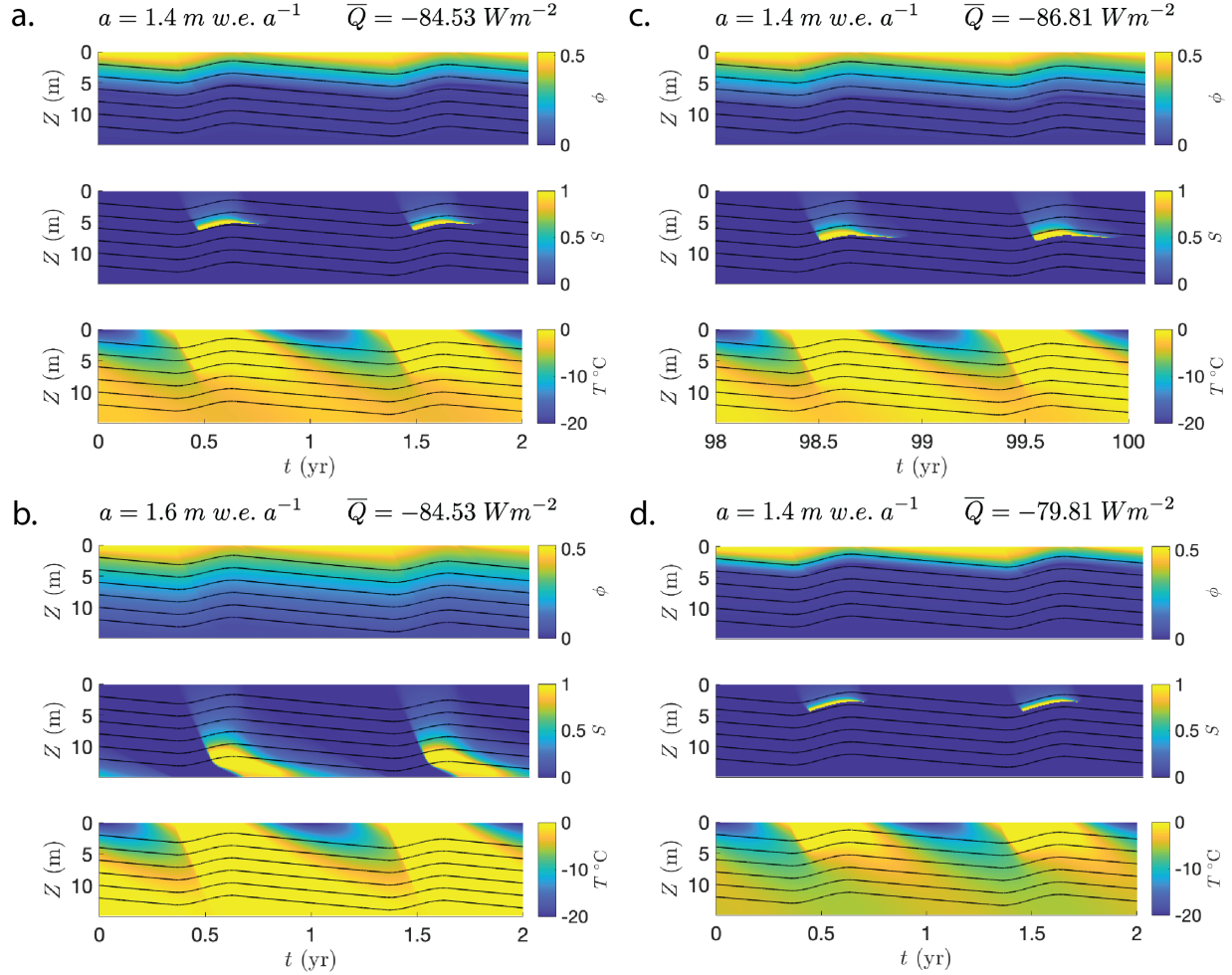
Figure 3.5. Space-time diagrams showing the evolution of porosity, saturation, and temperature as a function of time at Eclipse (a) and Divide (b) under mean temperature conditions, and at Eclipse under low (c) and high (d) temperature conditions. All simulations are run with a Q_0 value of 145 W m^{-2}. Above-freezing temperatures are maintained at depth year-round at Divide, enabling the presence of liquid water in the firn column. At Eclipse, surface energy conditions produce greater ablation but lower temperatures at depth in the firn column.

3.4.2 Melt Percolation

A second explanation for the incoherence of melt and temperature is that surface melt is able to percolate through multiple years' snowpack before refreezing. Based on my calculations of the energy requirement to raise the snowpack temperature to 0°C, it is possible for surface melt produced during high melt years at Eclipse to percolate into

41
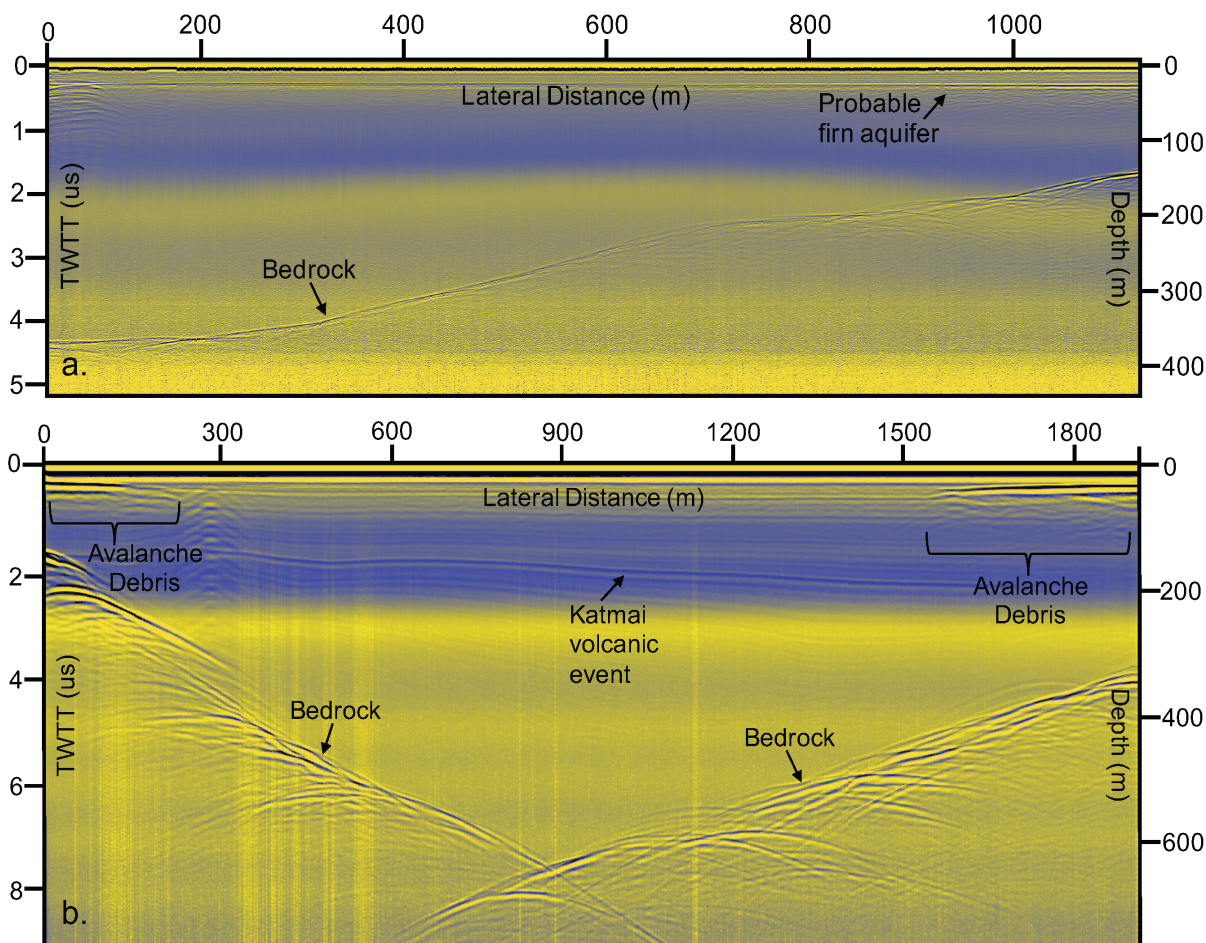
Figure 3.6. Surface-to-bedrock radar profiles at Divide (a) and Eclipse (b). Profiles at Divide and Eclipse were collected using 10 MHz and 5 Mhz antennae respectively. Prominent features (bedrock depth, avalanche debris, volcanic ash layer, high reflectance layer interpreted as a firn aquifer) are noted in both profiles. Two-way travel time is shown on the left axis, depth in the ice on the right axis, and lateral distance across-glacier along the top axis. Figure from McConnell (2019).

previous years' snow. Additionally, model results indicate that melt could percolate through to the previous year's snowpack under mean conditions at Eclipse (Fig. 3.4). Annual accumulation of 1.4 m w.e. equates to ∼3.2 m snow with a density of 440 kg m^{-3}, the average density value of surface snow (down to 1.3 m) at Eclipse. The 0°C warming front exceeds this depth during summer months, allowing interannual percolation during limited periods. However, because temperatures do not remain at or above freezing
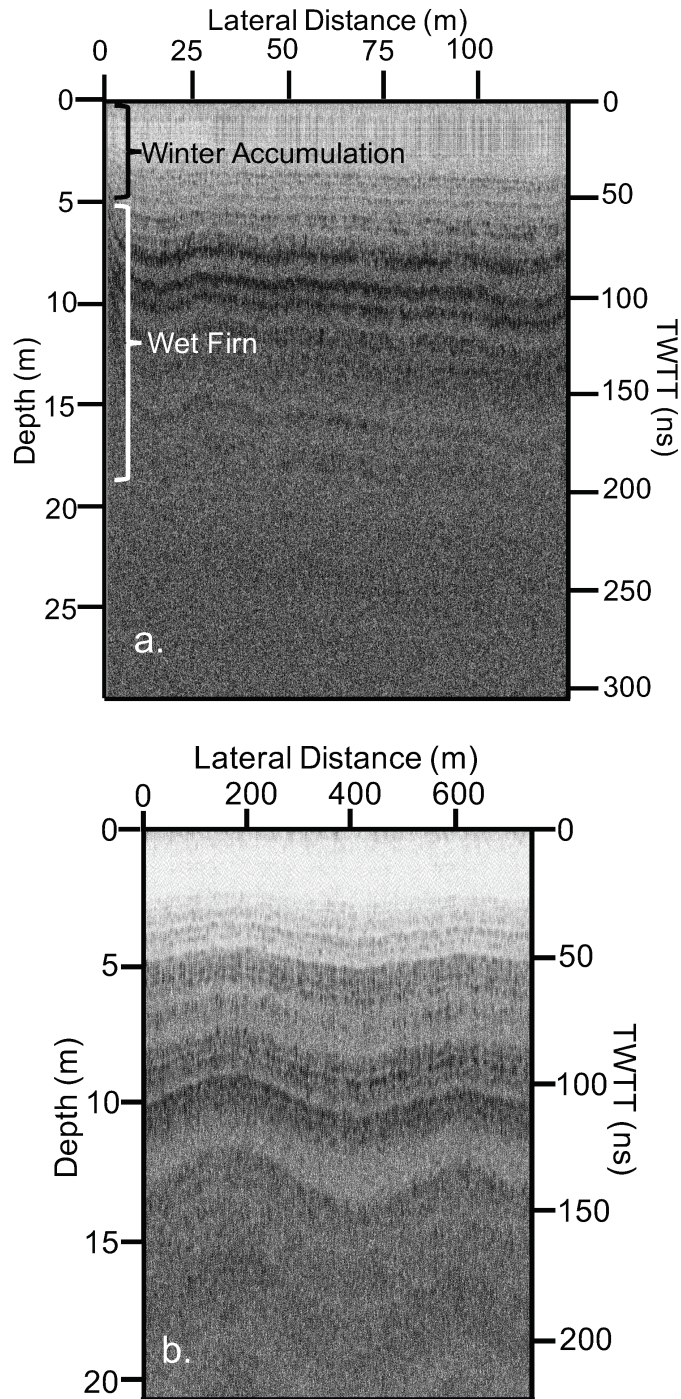
Figure 3.7. Shallow radar profiles at Divide (a) and Eclipse (b). Both profiles are collected using a 400 MHz antenna. Signal attenuation is greater at Divide, indicating higher water content than at Eclipse. Depth in the ice is shown on the left axis, two-way travel time on the right axis, and lateral distance across-glacier along the top axis. Figure from McConnell (2019).

year-round at any depth, liquid water cannot be stored perennially in the firn column and no firn aquifer develops at Eclipse. In contrast, firn below 10 m depth at Divide stays close to 0°C year-round under the same energy balance conditions (Fig. 3.5). This is likely due to the insulating effect of enhanced accumulation relative to Eclipse. In all seven simulations (varying the amplitude of prescribed surface energy balance), deep firn layers at Divide were better insulated and remained warmer than at Eclipse. A Q_0 value of 145 W m^{-2} most accurately reproduced differences in firn water content at the two sites observed using GPR, and was used for all end-member model runs.

The deeper penetration of the warming front under 2014 (cold) conditions than under 2016 (warm) conditions reflects the relative importance of meltwater and conduction as methods of downward heat transport in the firn column. Percolating meltwater far outstrips conduction in its efficacy at downward heat transport, so the temperature profile of the firn column is largely controlled by the degree to which melt can percolate. Although more melt is produced under 2016 conditions, its percolation is more limited for two reasons. First, the removal of a greater portion of the high-porosity surface snow layer by melt leaves a thinner layer through which melt can percolate with ease. Second, the refreezing of melt in the firn column more rapidly decreases its porosity, inhibiting the deeper percolation of subsequent melt. A greater portion of the firn column thus relies on conduction for heat transfer under 2016 conditions and remains cooler despite warmer surface temperatures. In neither end-member scenario does meltwater run off the surface. Rather, all melt produced refreezes in the firn column. The significant difference between the two scenarios is the depth at which enough refreezing occurs to inhibit further percolation. Both scenarios show the penetration of a seasonal warming front into snow from the previous year.

Despite generally capturing melt conditions at Eclipse and Divide, improvements upon this model are necessary to model years with high vs. low melt with enough accuracy to identify a threshold for interannual melt percolation. Specifically, accurate melt predictions

require the model to be forced directly with meteorological data rather than a prescribed sinusoid. A sinusoidal energy flux fails to fully capture the surface energy flux causing melt for two reasons. First, at overall cold locations, melt may only be produced on anomalously warm summer days, which would not necessarily be captured by a prescribed sinusoid. Additionally, prescribing the sinusoid using a mean annual energy flux fails to account for the distribution of higher-than-normal energy fluxes. Mean annual fluxes may increase due to increases in energy flux at any time of the year. However, only higher-than-normal summer fluxes will increase melt, as winter fluxes are generally well below the threshold for melt production.

3.4.3 Melt and Paleo Reconstructions

Layers of refrozen melt can provide a robust temperature proxy under the right conditions; however, percolation dynamics complicate melt-based reconstructions. To date, melt percolation has been largely approached as a single-threshold problem with two percolation scenarios separated by a single transition between them. Where surface temperatures only rarely reach above freezing, very little melt is produced and percolation is limited by melt supply. Under these conditions, discreet layers of refrozen melt may be directly related to surface temperature. In the single-threshold framework, with some degree of warming, enough melt is produced to percolate and/or run off the surface. At this point, discreet layers no longer refreeze, and melt cannot be used as a temperature proxy. Results here, however, suggest that melt percolation is actually a multiple-threshold problem with several distinct percolation regimes controlled by the relationship between surface temperature and snowpack insulation, which is largely dependent on accumulation rate. Given a constant accumulation rate, I propose four percolation regimes separated by three thresholds of surface temperature. At low surface temperatures (rarely above freezing), very little melt is produced, percolation is limited by supply, and discreet layers can be used as a temperature proxy. The low-temperature regime is exemplified by Mt.

Hunter, where a 400-year temperature record has been derived from melt layers (Winski et al. 2018). At lower-intermediate surface temperatures, enough melt is produced to percolate uninhibited to depth in the firn column (e.g. Eclipse mean conditions, Divide mean conditions, Eclipse 2014). Depending on how well insulated the melt is at depth, it may refreeze over the winter or remain liquid as a firn aquifer. Either way, extensive percolation has occurred and precludes the use of melt for temperature reconstruction. At upper-intermediate surface temperatures, so much melt is produced that its denuding of high-porosity surface snow and subsequent refreezing as impermeable ice layers prevents penetration of melt and warming to depth (e.g. Eclipse 2016). In the absence of extensive percolation, temperature information may potentially be gleaned from melt layers produced under these relatively high-melt conditions. Finally, at very high surface temperatures, enough melt is produced to run off the surface, and therefore cannot be used as a temperature proxy.

Modern melt layers at Eclipse appear to correspond to the lower-intermediate percolation regime. Although these cannot be used for temperature reconstructions, global temperatures during ~75% of the Holocene were lower than present (Marcott et al. 2013). Pre-modern melt layers at Eclipse may therefore remain useful as a temperature proxy. Based on GPR data, the ice at Eclipse approaches 600 m thickness toward the center of the icefield and likely contains a complete Holocene record, similar to nearby Mt. Logan (Fisher et al. 2004). However, interpretation of the Eclipse melt record should be undertaken with care as the site could transition between percolation regimes with modest temperature or accumulation changes. In particular, care should be taken with reconstructions during past periods of potential warmth such as the early Holocene (11.7-8.2 ka). The early Holocene thermal maximum (HTM) may have had an expression in the North Pacific region (Kaufman et al. 2004); however, published temperature records indicate variable conditions with no uniform regional warming (Kaufman et al. 2016). The early Holocene may in fact have been a cool period in some sectors of the North Pacific.

For example, glaciers in southern Alaska were in extended positions during the early Holocene relative to the middle Holocene (Kaufman et al. 2016). High-elevation temperatures in the St. Elias remain unknown during this period. Even when the percolation regime at Eclipse is poorly constrained, melt can still be used as a qualitative indicator of temperature. With sufficiently high temperatures for Eclipse to be in the lower- or upper-intermediate percolation regimes (no runoff), we would expect abundant melt in the ice core record. Although uncertainty about the percolation regime would preclude calculation of surface temperature, the presence of abundant melt would nonetheless indicate a period of temperatures near or above present levels.

3.5 Conclusions

Despite the demonstrated potential of ice core melt layers at many sites in summer temperature reconstructions, I find that melt layers in the Eclipse 2016 ice core do not reflect summer temperatures on the icefield. Years of high melt in the record do not coincide with years of high summer temperatures, either due to complicating environmental factors driving melt production, or melt percolation distorting the record. Given the dominance of temperature in driving surface energy balance and melt, and the fidelity of the ablation-temperature relationship across surface conditions (including at nearby Divide), it is most likely that the percolation rather than production environment is responsible for the incoherence of melt and high PDDs at Eclipse. Meyer and Hewitt's model also suggests a complex relationship between melt production, percolation, and refreezing. Under high-melt conditions, melt percolation and the penetration of a seasonal warming front into the snowpack are actually more restricted than under low-melt conditions, likely due to the rapid decrease in firn porosity with extensive refreezing. My results suggest that melt percolation is a multiple-threshold problem, with thresholds controlled by the relationship between surface temperature and snowpack insulation (i.e. accumulation). Modern melt layers at Eclipse do not correspond to years of high

47

temperatures; however the site may yet contain a viable record of past temperatures under mostly cooler Holocene surface conditions.

CHAPTER 4

BUBBLE ANALYSIS IN THE MT. HUNTER ICE CORE

4.1   Background and Goal

Ice cores provide some of the highest resolution records available of past climate, in particular past temperature, which can be derived through stable isotope concentrations or through melt layers. Melt layers present an especially robust way to reconstruct past temperatures due to the direct physical link between surface temperatures and their production. Melt layers form when surface melt resulting from high temperatures percolates through the snowpack before refreezing at the 0°C isotherm (Pfeffer and Humphrey 1998). By measuring the amount of water contained in a melt layer, it is possible to calculate how much energy was needed to produce the layer, and thereby infer the surface temperature at the time of production. Modern warming in the North Pacific is unprecedented in the past 400 years, as evidenced by a melt record from Mt. Hunter (Alaska Range); however, preliminary observations of older ice in the Hunter core suggest intense melt production during past periods of global warmth such as the Medieval Climate Anomaly (MCA, roughly 950-1250 C.E.; Winski et al. 2018). Understanding the relationship between climate, temperature change, and glacier mass balance during past periods of warmth such as the MCA may provide insight into regional forcing and feedback mechanisms contributing to modern glacier mass loss. Unfortunately, older melt estimates are uncertain as there are notable challenges to identifying melt layers using established optical techniques after they have undergone a high degree of strain and vertical thinning (Winski et al. 2018). Older melt layers therefore present an as yet untapped source of information on past periods of warmth, information that becomes increasingly pertinent as we look to predict impacts of rising temperatures today. Here, I apply a novel melt analysis technique to the deep portion of an ice core taken from Mt. Hunter (Alaska Range) and investigate the limitations of melt layer preservation at depth in the core.

The goal of this chapter is to identify melt layers at depth in the Hunter core after they have undergone a high degree of strain. I hypothesize that layers of refrozen melt can be identified by their bubble number density, even when they have been thinned to 5-10% of their original thickness. To address my hypothesis, I answer the following questions:

1. Does the bubble density of refrozen melt differ significantly from that of unaltered ice?

2. Do ambiguous features at depth more closely resemble refrozen melt or unaltered ice in their bubble density profiles?

4.2   Methods

4.2.1   Ice Core Collection, Processing, and Dating

Two ice cores were collected in 2013 from the summit plateau on Mt. Hunter (62.93°N, 151.08°W, 3,910 m a.s.l.) in Denali National Park, Alaska (Winski et al. 2017). The cores were drilled on the saddle between Hunter's north and middle peaks (Winski et al. 2017). Each core was 8 cm in diameter and drilled to bedrock (208 m) using a Badger-Eclipse ice drill (Winski et al. 2017). After retrieval, the cores were shipped to the National Ice Core Laboratory in Denver, Colorado (Winski et al. 2017). There they were weighed, measured for density calculations (∼1 m resolution), and cut into 3 x 3 cm sticks for melting at Dartmouth (Winski et al. 2017). Ice not used for melting at Dartmouth was used in this study for thin section analyses. The timescale for the Hunter core was developed using annual layers independently counted by three researchers (D. Winski, E. Osterberg, D. Ferris; Winski et al. 2017). Annual oscillations in δ^{18}O, melt layers, magnesium, dust, liquid conductivity, ammonium, and methanesulfonic acid were used to delineate layers back to 1777 CE (Winski et al. 2017). δ^{18}O, δD, deuterium excess, dust and liquid conductivity were used to develop the timescale from 1777 to 1500 CE (Winski et al. 2017). The timescale from 1500-800 CE is based exclusively on conductivity and dust

concentration (Winski et al. 2017). Volcanic peaks in sulfate, chloride and conductivity were used to validate the ice core chronology (Winski et al. 2017). A complete description of the laboratory procedures and timescale development for the Hunter cores can be found in Winski et al. (2017).

4.2.2 Bubble Density Analysis

My approach was to quantify bubble number density in ice from the Hunter core by examining the ice in thin section. Following visual inspection of the core, sections of ice containing melt layers and ambiguous features were visually identified and recorded. Here I use the term 'melt layer' to refer to a discrete layer of refrozen melt as visually identified by its color (darker than that of the surrounding ice). I use the term 'unaltered ice' to refer to ice that is uniform in color and shows no evidence of refrozen melt. I use the term 'ambiguous feature' to refer to a section of ice which may appear slightly darker than the surrounding ice, but for which the difference is too subtle to confidently identify the feature as a melt layer. Pucks of ice were cut from sections of unaltered ice, as well as from sections containing melt layers and ambiguous features. Thin sections approximately 1 cm thick were cut from each puck using a bandsaw. Thin sections were oriented lengthwise along the puck, so that they represent a range of depths (times) rather than a single discrete depth (time) (Fig. 4.1). The thin sections were then filed to a thickness of approximately 1 mm using a microtome blade and polished using fine grit sandpaper.

The 1 mm thin sections were photographed over a light table five times between crossed polarized lenses, with the lenses at five different angles. They were also photographed twice without crossed polarized lenses, with the light table at two different brightness settings. All the photographs were then examined manually to determine which settings produced the clearest images of bubbles in the ice. The two polarized photographs for each sample that most clearly showed bubble outlines were selected for image analysis. Two photographs were used to mitigate any bias that might arise from differences in contrast
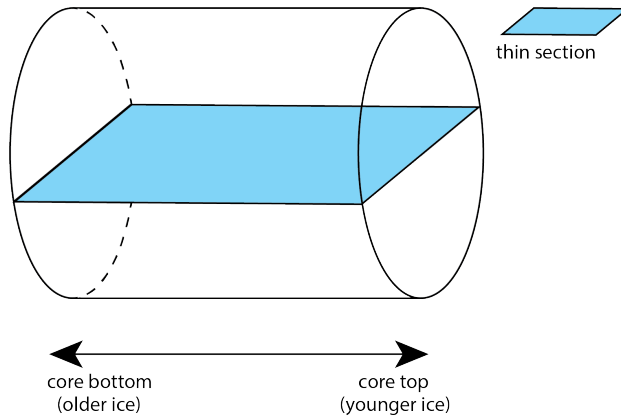
Figure 4.1. Thin section cut lengthwise along puck of ice. Blue plane indicates thin section.

between the bubbles and surrounding ice among different ice crystals due to birefringence, as well as bias from difficulty in identifying bubbles along high-contrast grain boundaries. The brighter of the two unpolarized photographs was selected for image analysis, due to the high contrast between bubble edges and surrounding ice. Photographs taken with crossed polarizers allowed me to distinguish among grains in the ice. Photographs taken without crossed polarizers eliminated any bias arising from birefringence and from high-contrast grain boundaries.

In each photograph selected for analysis, the bubbles were digitized as black ellipses (Fig. 4.3b). In the polarized photos, this was done manually using Adobe Illustrator. In the unpolarized photos, the digitization was semi-automated using Matlab's Canny method edge detect algorithm. Features identified by the algorithm were then filtered by eccentricity (features with an eccentricity >0.9 were removed) to eliminate cracks and scratches that were erroneously identified as bubbles. The preliminary bubble map was imported into Adobe Photoshop, where additional erroneously identified bubbles were manually erased and bubbles missed by the edge detect algorithm were manually added.

The fraction of black pixels (bubble pixels) in each column of pixels of the resultant binary bubble maps was calculated, and pixel columns were converted to depth in core using sample top and bottom depth measurements.

4.3 Results

In two of the three samples with optically confirmed melt layers, bubble number density does decrease within the uncertainty of where the melt layer was measured to be (Fig. 4.2; discussed in section 4.4). However, bubble number density shows no obvious decrease in the samples with ambiguous features.

4.4 Discussion

4.4.1 Pixel Brightness and Bubble Number Density

Although the thin section bubble density data is too noisy to classify ambiguous features as melt or unaltered ice, results for samples containing previously identified melt layers agree with optical identification of these layers (Fig. 4.3). This study therefore supports the assumption that pixel brightness in full core photographs does indeed reflect bubble number density, providing a physical basis for optical identification techniques and implying that further development of bubble density measurement methods is worthwhile for quantifying the amount of melt in an ice core. Based on these results, I make two recommendations for further work to develop ice core melt layers as a temperature proxy. First, I suggest that pixel brightness continue to be used as a proxy for bubble number density, but that it be spot checked with periodic bubble fraction datasets from thin sections. Rather than making one thin section for every optically identified melt layer, I recommend making several thin sections for a few select melt layers distributed along the core and stacking the resultant data for each layer to improve the signal-to-noise ratio. The stacked data can then be used to verify whether pixel brightness does reflect bubble density throughout the core as melt layers undergo thinning.

4.4.2 Full Diameter Samples

Second, I recommend the continued improvement of techniques for measuring bubble number density independent of pixel brightness. This study presents two primary areas for
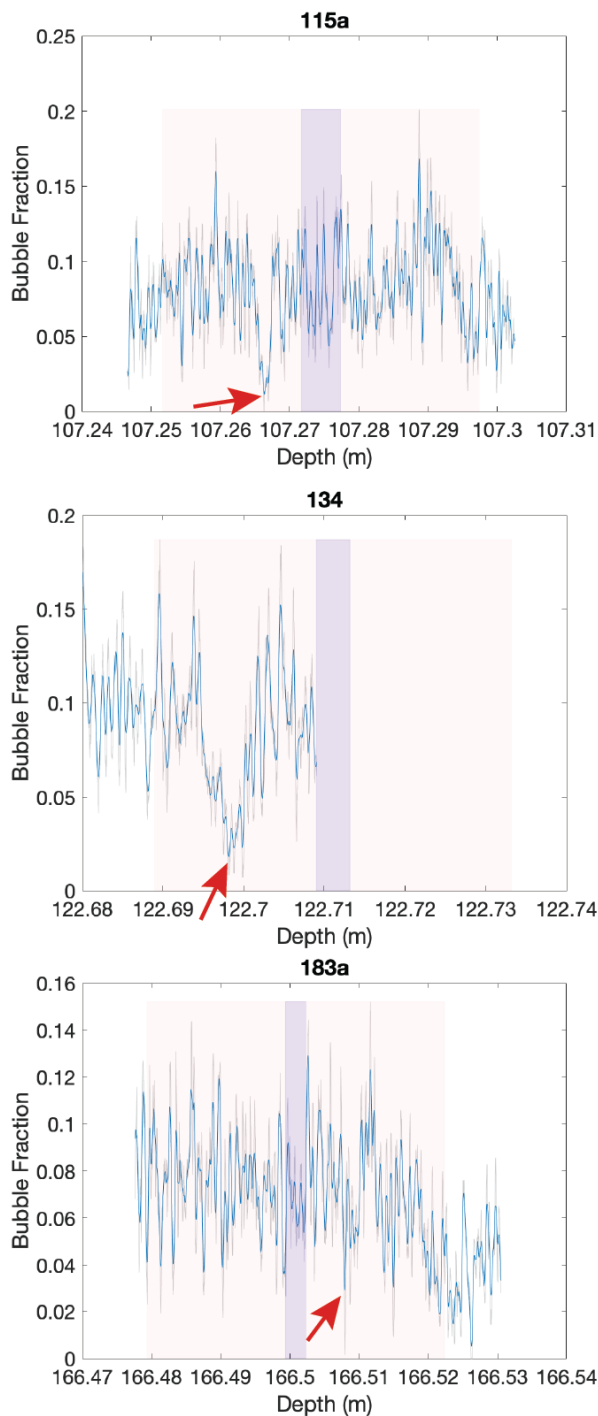
Figure 4.2. Bubble fraction data from thin sections with optically identified melt layers. Red arrows indicate melt layer position identified in thin sections. Transparent Purple bars indicate depth of optically identified melt layer in full core photographs. Transparent red shading indicates uncertainty in melt layer depth in thin section arising from error introduced during thin section production. Sample 134 has a larger range of uncertainty because trimming of the thin section was not uniform. Melt layers identified in thin section are offset, but within error, from those identified in full core photographs.
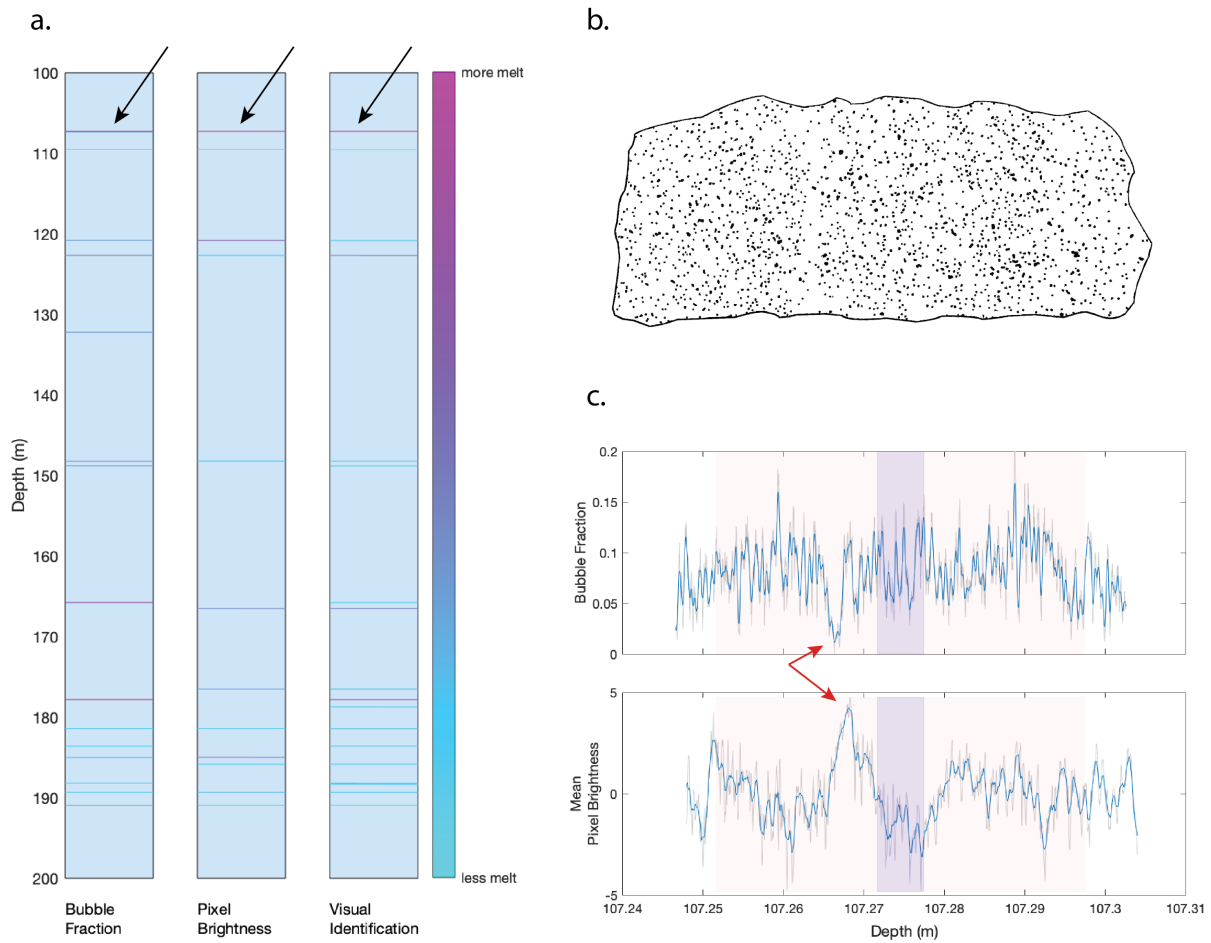
Figure 4.3. Relative magnitude of melt layers at 100-200 m depth from different analytical techniques (a), digitized bubble map of thin section 115a (b), and bubble fraction and detrended mean pixel brightness along thin section 115a (c). Melt layers in panel (a) are quantified based on bubble fraction, pixel brightness, and visual identification in full core photos. The location of thin section 115a (shown in panels (b) and (c)) is indicated by black arrows on core diagrams in panel (a). Red arrows indicate melt layer position identified in thin sections. Transparent Purple bars indicate depth of optically identified melt layer in full core photographs. Transparent red shading indicates uncertainty in melt layer depth in thin section arising from error introduced during thin section production. Melt layers identified in thin section are offset, but within error, from those identified in full core photographs.

further improvement: (1) decreasing the amount of noise in bubble number density data, and (2) increasing precision of depth measurements for individual samples. The noise in the bubble number density data likely arises from my use of two-dimensional thin sections to represent the three-dimensional distribution of bubbles in an ice core, and from the binarization of thin section images. Previously established optical identification techniques use photographs of ice cores at their full thickness (diameter of 8 cm), thereby stacking the data from eighty 1 mm thin sections, reducing noise and amplifying the melt signal. When optical techniques are used on thin section photographs, the resultant data shows similar levels of noise to our bubble fraction data, supporting our proposition that using full-diameter samples effectively reduces noise in the data (Fig. 4.4).

Studying full-diameter samples would also eliminate a number of sources of error introduced into our depth measurements by the thin section production process. First, thin sections were cut from pucks of ice, which themselves were not always cut perfectly horizontally across the ice core. Moreover, not all pucks were bounded by cuts on both ends; some were bounded by a break in the core. In these cases, the puck was not a uniform length across its diameter, and the top and bottom depths of a thin section cut from such a puck could have up to 2 cm of uncertainty. Occasionally, thin sections required trimming with a microtome blade before being mounted on a glass slide. Trimming introduced another few millimeters of uncertainty, as the trim was not always perfectly vertical. Lastly, the droplets of water used to adhere the thin section to the glass slide introduced additional uncertainty. Water intrusion around the edges of the thin section was difficult to constrain, even with care taken to plane the section as horizontal as possible prior to mounting. The effects of water intrusion could be mitigated by demarcating the sample top and bottom edges on the glass slide prior to filing the sample down, but a few millimeters of error were still introduced, as the demarcation had to be bold enough to show up in backlit photographs.
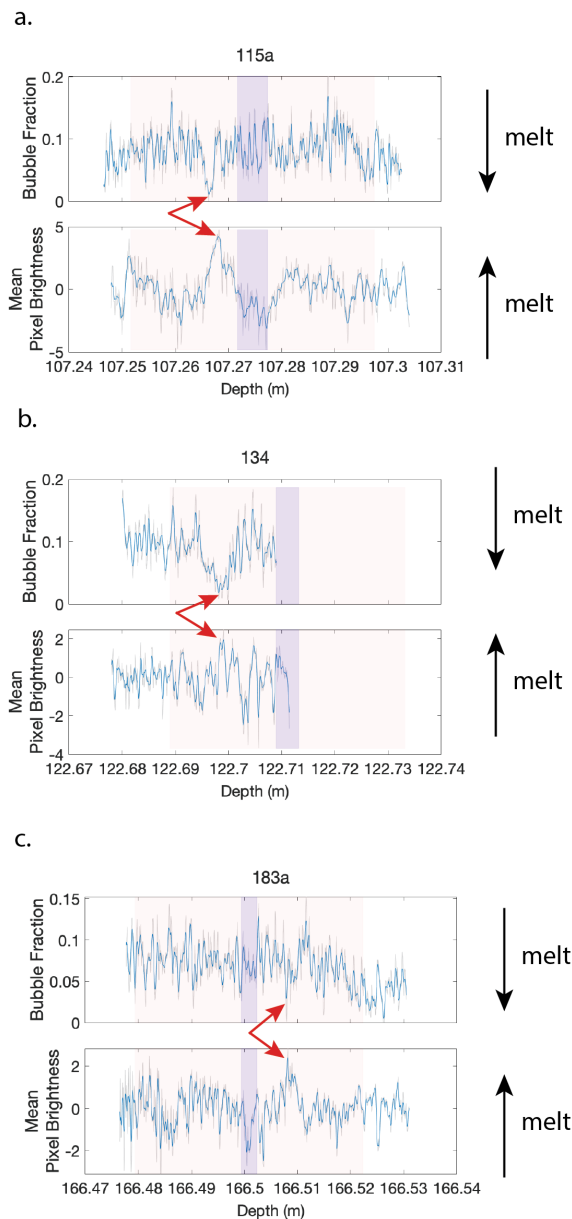
Figure 4.4. Pixel brightness and bubble fraction data from thin sections 115a (a), 134 (b), and 183a (c). Pixel brightness data show peaks corresponding to dips in bubble fraction. Both pixel brightness and bubble fraction data from individual thin sections are characterized by a low signal-to-noise ratio. Red arrows indicate melt layer position identified in thin sections. Transparent purple bars indicate measure melt layer depth as measured in full core photographs. Transparent red shading indicates uncertainty in melt layer depth in thin section arising from error introduced during thin section production. Sample 134 has a larger range of uncertainty because trimming of the thin section was not uniform.

4.4.3 Suggested Analytic Techniques

Two techniques that use full-diameter core samples and show promise in their application to bubble density studies are continuous density measurements (Breton, Hamilton, and Hess 2009) and Laser-Light Scattering (LLS) (Stolz and Ram 2005). Not only could both of these techniques be used on full-diameter samples (reducing the noise in resultant bubble number density data), but they could also be performed continuously along the core (eliminating the need for discreet thin sections and reducing uncertainty in depth measurements). Continuous density measurements can be obtained using the Maine Automated Density Gauge Experiment (MADGE) system, which compares the transmission rate (intensity) of a beam of γ-rays through a sample with the intensity of the same beam passing through air (Breton, Hamilton, and Hess 2009). Once corrected for changes in density downcore due to compression of the ice over time, changes in ice core density should reflect changes in the air content, or bubble density, of the core. MADGE's highly accurate, automated measurements can be taken at a high spatial resolution continuously along the ice core, eliminating some of the uncertainties associated with thin section production and analysis. The MADGE system introduces uncertainty in the measurement of sample thicknesses using calipers, as well as in the correction for detection system dead time, which is the period of time following the arrival of one γ-ray when the system is unable to detect newly arriving γ-rays (Breton, Hamilton, and Hess 2009). Limited uncertainty is also introduced by the use of deionized water for calibration, as natural ice contains impurities; but empirical studies have shown the pure-ice assumption to be reasonable for γ-ray measurements, and resulting uncertainty to be negligible relative to other sources (Breton, Hamilton, and Hess 2009).

LLS measures the scattering of light by an ice core to determine the concentrations of different light-scattering features within it. LLS has previously been used to measure dust concentrations in ice cores; however, where present, bubbles have been found to dominate over dust as light-scatterers (Stolz and Ram 2005). LLS has four advantages over thin

section analysis. LLS is fast, repeatable, non-destructive, and can be done continuously (Stolz and Ram 2005). In contrast each thin section takes hours of preparation, there is not always enough ice for replicate thin sections should one be contaminated, production of thin sections requires destruction of the core, and it can only be done for discreet samples. Use of LLS requires knowledge of the depth at which air clathrates form in the ice and the pressure relaxation processes that transform clathrates back into bubbles once the ice core is extracted (Stolz and Ram 2005). In relatively shallow alpine cores such as the Hunter core, air clathrates are not a concern, as adequate pressures for their formation are not reached; observations of clathrates have been restricted to the deeper parts of polar ice sheets (e.g. below 500 m at Vostok, below 900 m at GRIP) (Kuhs, Klapproth, and Chazallon, n.d.; Kipfstuhl et al. 2001). LLS can be used to infer both bubble number density and median size of bubbles in an ice core (Stolz and Ram 2005). Bubble number density is calculated using mass transmissivity and mass density, and median bubble size can be inferred with the assumption of spherical bubbles, which is a reasonable assumption under strain rates low enough for diffusive processes to effectively oppose elongation (Stolz and Ram 2005; Alley and Fitzpatrick 1999). In the Hunter core samples used in this study, the mean aspect ratio of bubbles is approximately 1.35.

4.5   Conclusions

I found that bubble number density results for melt layers compared with unaltered ice agree with established optical identification techniques, thereby providing a physical basis for their continued use. Bubble number density in ice core thin sections cannot be used to unequivocally identify melt layers; it does not differ significantly between melt layers and unaltered ice because of a low signal-to-noise ratio in the thin section data. However, bubble number density on full thickness core samples provides an opportunity for further development of the melt layer summer temperature proxy. Continuous density measurements and Laser-Light Scattering are two techniques that hold potential for

quantifying bubble number density on full core samples. If successful, either of these methods would improve the signal-to-noise ratio in bubble number density data and eliminate uncertainties in depth introduced by the thin section production process.

CHAPTER 5

CONCLUSIONS AND FUTURE WORK

5.1 Summary of Findings

My aim in this thesis was to examine past and present temperature trends in the North Pacific region and their relationship to glacier mass balance. In Chapter 2, I evaluated three potential causes of a cold bias in MODIS LSTs in the St. Elias Range. I found that the MODIS cold bias is most pronounced under conditions that favor near-surface temperature inversions, namely low wind speeds and low levels of incoming solar radiation. This suggests a physical temperature difference between the snow surface and air in the St. Elias. I also found that neither MODIS' large spatial footprint in highly heterogeneous terrain nor poorly constrained emissivity values fully explain the bias. Although heterogeneity in surface type and properties does occur over MODIS' 1 km^2 footprint, the coherence of temperatures at Eclipse and Divide (30 km apart, 400 m difference in elevation) suggests that a cold bias in excess of 10°C would be unlikely to result from heterogeneity within a single square kilometer. Moreover, surface temperatures from ASTER display a similar cold bias relative to in situ measurements despite ASTER's smaller footprint (90 m). Additionally, I found a greater bias in fall and winter relative to spring and summer to be present in both MODIS LSTs and brightness temperatures, which have not yet taken emissivity into account. The cold bias thus is not introduced by the incorporation of emissivity. However, poorly constrained emissivity values cannot be ruled out as an exacerbating factor, particularly following snowfall events, when emissivity is likely to rapidly evolve as a result of settling and compaction processes. Emissivity changes after snowfall events may contribute to the larger wintertime bias, as snowfall events occur more frequently in the winter; however, the temporal resolution of MODIS data is not high enough to examine the response of the cold bias to individual snowfall events. In short,

emissivity values do not introduce the MODIS cold bias, but their importance in amplifying it remains unknown.

In Chapter 3, I examined the relationship between summer temperatures and melt layer production and preservation at Eclipse Icefield. I found that years of high melt in the ice core record do not coincide with years of high temperatures at the surface. I also found that years of high ablation at nearby Divide do coincide with years of high surface temperatures, suggesting that complex percolation dynamics, rather than the surface environment, are responsible for the incoherence of melt and temperature at Eclipse. Meyer and Hewitt's melt percolation model also indicates a complicated percolation environment, with the extent of percolation controlled by the relationship between surface temperature and snowpack insulation. Model results suggest that melt percolation is a multiple-threshold problem. At low surface temperatures, melt percolation is limited by melt supply. At lower-intermediate surface temperatures, extensive percolation is supported by the insulation of deeper snowpack layers from annual surface cooling. At upper-intermediate surface temperatures, enough melt is produced to remove the insulating layers of surface snow and decrease the porosity of the firn column enough to inhibit melt penetration to depth. Finally, at very high surface temperature, melt begins to run off the surface rather than exclusively percolate.

In Chapter 4, I quantified bubble number density in an ice core drilled at Mt. Hunter in order to distinguish refrozen melt layers from unaltered ice. Established optical techniques for melt layer identification rely on the assumption that the brightness of a backlit ice layer reflects the density of air bubbles in the ice; however, these techniques cannot be used on deep layers that have undergone considerable vertical strain. I found that bubble number density for melt layers compared with unaltered ice agree with establish optical techniques, validating their continued use. Bubble number density measured in ice core thin sections cannot be used to unequivocally identify melt layers because of a low signal-to-noise ratio;

however, the method shows promise with further development of bubble number density techniques on full-thickness core samples.

5.2   Broader Implications and Significance

Despite lingering uncertainties about the source of the MODIS LST cold bias, it is apparent the bias is most extreme in the fall and winter and relatively inconsequential during the summer melt season. This means that MODIS LSTs can be used to qualitatively examine summer temperature trends and their impact on glacier mass balance in the St. Elias. The results here may be relevant to other glaciated areas as well. Many heavily glaciated regions are remote and difficult to access for in situ measurements, so the utility of MODIS LSTs in tracking melt season temperature changes is noteworthy. In addition, the persistence of a cold bias across spatial scales and in brightness temperatures as well as LSTs suggests that the bias is a physical difference between surface and air temperature rather than an artifact of instrumentation. A near-surface temperature inversion could have marked effects of surface processes including melt production. These results are therefore pertinent not only to the continued use of MODIS LSTs to track temperature changes, but also to constraining melt production and other surface processes at Eclipse.

The incoherence of melt and temperature at Eclipse over the available modern record appears to be the result of complex melt percolation dynamics at the site and precludes the use of melt-based temperature reconstructions under current site conditions. However, under the cooler conditions present through much of the Holocene, percolation may have been limited by melt supply at Eclipse and resultant melt layers may yet provide a valuable temperature record. Results here highlight the importance of snow hydrology for climate reconstructions. Complex percolation dynamics may influence not only the preservation of melt layers, but also of glaciochemical signals such as stable water isotopes and trace elements. Percolation regime should therefore be considered when selecting future ice core sites for paleoclimate reconstructions.

The agreement of bubble number density with optical melt layer identification validates the use of optical identification techniques as a proxy for bubble number density in ice cores. Additionally, bubble number density provides evidence of past periods of warmth even if we do not have the necessary resolution to quantify temperature or precisely date these periods. This indicates that ice in the North Pacific has survived past warm periods and justifies continued efforts toward quantifying past high temperatures and glacier response in the region.

5.3 Future Directions

Although my results provide insight into potential sources of the MODIS cold bias, further work is needed to identify its cause. Specifically, I suggest a number of in situ measurements be taken. First, I suggest paired in situ measurements of surface and 2 m air temperature to determine whether there is a physical temperature difference between the two that is responsible for the bias. Second, I suggest in situ measurements of emissivity and surface properties (e.g. grain size, wetness) following individual snow events to examine the response of snow surface emissivity to snowfall and subsequent processes. Results from the Eclipse melt record indicate a complex melt production and percolation environment. Additional work is necessary to elucidate the extent of melt preservation at Eclipse and the impact of melt on ice core geochemistry. Bubble number density shows promise as a melt layer identification method if analytical techniques can be developed for full-thickness samples. Continuous density measurements and Laser-Light Scattering are two approaches that may be applicable to quantifying bubble number density on full-thickness samples. If successful, either method would improve the signal-to-noise ratio in the resultant data and mitigate uncertainties in layer depth introduced during production of thin sections.

APPENDIX A

TIR BAND WAVELENGTHS

Table A.1. Wavelengths of the thermal infrared (TIR) bands used in this study.

Instrument	Band	Wavelengths (μm)
MODIS	31	10.780-11.280
	32	11.770-12.270
ASTER	10	8.125-8.475
	11	8.475-8.825
	12	8.825-9.275
	13	10.25-10.95
	14	10.95-11.65
Landsat 4-7	6	10.40-12.50
Landsat 8	10	10.60-11.19
	11	11.50-12.51

APPENDIX B

FORCING ENERGY FLUX

I calculated the forcing energy flux from meteorological data at Divide using the following equation from Meyer and Hewitt 2017:

$$Q(t) = (1 - \alpha)S_w + L_w - \epsilon\sigma T_m{}^4 - \chi(T_a - T_m) + \rho_w c_i a(T_a - T_m) + \rho_w c_w R(T_a - T_m) \quad \text{(B.1)}$$

where α is albedo, ϵ is emissivity, σ is the Stefan-Boltzmann constant, T_m is the melting temperature of ice, χ is the turbulent heat transfer coefficient, T_a is the air temperature, ρ_w is the density of water, c_i is the specific heat of ice, a is the accumulation rate, R is rainfall. S_w and L_w are incoming shortwave and longwave radiation, which were calculated according to the methods outlined by Brock and Arnold (2010). Numerical values used in the calculation of the forcing energy flux are listed in Table B.1 . Air temperatures are input from Divide weather station data.

I then calculated the mean forcing energy flux for all years with complete data (2014-2019). I input the mean value (-84.53 W m^{-2}) as $\overline{Q}$ into my prescribed sinusoidal energy flux. The amplitude of my calculated energy flux varied from approximately 130 W m^{-2} to 160 W m^{-2}. I ran seven simulations under mean conditions at Eclipse and Divide using Q_0 values from 130 to 160 W m^{-2} in intervals of five (130 W m^{-2}, 135 W m^{-2}, 140

Table B.1. Numerical values used in the calculation of the forcing energy flux

α	0.8	albedo
ϵ	0.97	emissivity
σ	$5.6 \cdot 10^{-8}$ W m^{-2} K^{-4}	Stefan-Boltzmann constant
T_m	273.15 K	Melting temperature of ice
χ	10.3 W m^{-2} K^{-1}	Turbulent heat transfer coefficient
ρ_w	1000 kg m^{-3}	Density of water
c_i	2.05 kJ kg^{-1} K^{-1}	Specific heat of ice
a	1.4 m w.e. a^{-1}	Accumulation rate
c_w	4.814 kJ kg^{-1} K^{-1}	Specific heat of water
R	0 m w.e. a^{-1}	Rainfall

W m^{-2}, 145 W m^{-2}, 150 W m^{-2}, 155 W m^{-2}, 160 W m^{-2}). I selected an amplitude of 145 W m^{-2} for subsequent model runs because it best recreates the distinction between Divide and Eclipse melt percolation in response to a higher accumulation rate at Divide. Namely, Divide has an annual accumulation rate of 1.6 m w.e. and develops a firn aquifer. Eclipse has an annual accumulation rate of 1.4 m w.e. and does not develop a firn aquifer.

BIOGRAPHY OF THE AUTHOR

Ingalise Kindstedt was born in Burlington, Vermont on March 29, 1997. She grew up in Shelburne, Vermont and graduated from Champlain Valley Union High School in 2015. She attended Georgetown University, where she earned her Bachelor of Science in Foreign Service, specializing in the intersection of science, technology, and international affairs. While at Georgetown, she spent some time working as a research assistant at the United States Geological Survey in Reston, Virginia. Upon her graduation in 2019, Inga entered the Quaternary and Climate Studies program at the University of Maine Climate Change Institute. After receiving her Master's degree, she plans to continue her studies at the University of Maine and earn her Doctorate. In her free time, Inga enjoys taking advantage of all the outdoor recreation Maine has to offer. You can find her skiing as long as there is snow on the ground, climbing whenever there isn't, and fitting in hikes and paddles in between. Ingalise Kindstedt is a candidate for the Master of Science degree in Quaternary and Climate Studies from the University of Maine in May 2021.